

# A Quantum Dot Heterojunction Photodetector

by

Alexi Cosmos Arango

Submitted to the Department of Electrical Engineering and Computer  
Science

in partial fulfillment of the requirements for the degree of

Masters of Science in Computer Science and Engineering

at the

MASSACHUSETTS INSTITUTE OF TECHNOLOGY

February 2005

© Massachusetts Institute of Technology 2005. All rights reserved.

Author .....  
Department of Electrical Engineering and Computer Science  
November 2004

Certified by .....  
Vladimir Bulović  
Associate Professor, KDD Career Development Chair  
Thesis Supervisor

Accepted by .....  
Arthur C. Smith  
Chairman, Department Committee on Graduate Students



# A Quantum Dot Heterojunction Photodetector

by

Alexi Cosmos Arango

Submitted to the Department of Electrical Engineering and Computer Science  
on November 2004, in partial fulfillment of the  
requirements for the degree of  
Masters of Science in Computer Science and Engineering

## Abstract

This thesis presents a new device architecture for photodetectors utilizing colloiddally grown quantum dots as the principle photo-active component. We implement a thin film of cadmium selenide (CdSe) quantum dot sensitizers, sandwiched between an electron-transporting titanium dioxide ( $\text{TiO}_2$ ) layer and a hole-transporting N,N'-diphenyl-N,N'-bis(3-methylphenyl)-(1,1'-biphenyl)-4,4'-diamine (TPD) organic small molecule layer. The wide band gap  $\text{TiO}_2$  and TPD layers are found to block charge injection under reverse bias, yet serve as transport layers for photo-excited charge generated in the CdSe. The internal quantum efficiency is approximately 1% at zero bias and saturates at 3% at -1V. Current-voltage sweeps yield low dark current in reverse bias and significant hysteresis under illumination. We speculate that the hysteresis and low quantum efficiency are due to charge accumulation at the  $\text{TiO}_2/\text{CdSe}$  interface.

Thesis Supervisor: Vladimir Bulović

Title: Associate Professor, KDD Career Development Chair



# Acknowledgments

I am foremost indebted to my cheerful advisor, Vladimir Bulović, who is an extraordinarily supportive and thoughtful professor.

I would like to thank professor Mounqi Bawendi and David Oertel, our collaborators who supplied the quantum dot material for this work. I especially thank David for his commitment, helpful discussions and skill in preparing quantum dot films.

I would also like to thank the dedicated graduate students and post-docs who spent years building the device growth capabilities at LOOE, namely Debbie Mascaro, Conor Madigan, Seth Coe-Sullivan and John Kymissis. Conor deserves special mention for proofreading drafts of this thesis.

I am particularly indebted to my friends and housemates Liza Marcato, Bénédicte Mornet, PJ Barry, Ryan Redmond, Ingrid Werge and Todd Freehafer, who nourished me with their fine home cooking and companionship for so many years.

Finally, I'd like to thank my parents for their support and encouragement.

This research was generously supported by the Institute for Solder Nanotechnology (ISN).



# Contents

<b>1</b>	<b>Introduction</b>	<b>15</b>
1.1	Introduction to photodetectors . . . . .	16
1.1.1	Photodetector performance . . . . .	16
1.2	Low-dimensional semiconductors . . . . .	20
1.2.1	Quantum well infrared photodetectors . . . . .	22
1.2.2	Quantum dot infrared photodetectors . . . . .	23
1.3	Colloidal quantum dot technology . . . . .	24
1.3.1	Colloidal quantum dot photodetectors . . . . .	24
1.4	Our device concept . . . . .	26
1.5	Structure of thesis . . . . .	26
<b>2</b>	<b>Theoretical background and photodetector design considerations</b>	<b>27</b>
2.1	Ideal p-n junction diode . . . . .	27
2.1.1	Description of the p-n junction . . . . .	28
2.1.2	Equivalent circuit model under illumination . . . . .	30
2.2	Semiconducting metal oxides . . . . .	31
2.2.1	Electron-accepting $\text{TiO}_2$ . . . . .	33
2.2.2	$\text{TiO}_2$ in photovoltaic devices . . . . .	34
2.3	The CdSe quantum dot film . . . . .	36
2.4	Organic semiconductors . . . . .	37
2.4.1	The organic hole transport molecule TPD . . . . .	39
2.5	Our device architecture . . . . .	39
2.5.1	The concept of blocking layers . . . . .	40

2.6	Summary . . . . .	42
<b>3</b>	<b>Device fabrication</b>	<b>43</b>
3.1	The TiO <sub>2</sub> layer . . . . .	43
3.1.1	Solgel deposition of TiO <sub>2</sub> films . . . . .	44
3.1.2	Radio frequency sputter deposition of TiO <sub>2</sub> films . . . . .	45
3.2	The CdSe layer . . . . .	46
3.3	Purification of organic small molecules . . . . .	47
3.4	The complete device growth process . . . . .	47
3.5	Probe fixture and patterning . . . . .	50
3.6	Summary . . . . .	50
<b>4</b>	<b>Current-voltage characteristics under illumination</b>	<b>53</b>
4.1	Measurement apparatus . . . . .	53
4.1.1	Measurement in atmosphere . . . . .	53
4.1.2	Measurement in nitrogen . . . . .	55
4.1.3	Sign convention . . . . .	56
4.2	Experimental results . . . . .	57
4.2.1	Characteristics of control devices without a quantum dot film	57
4.2.2	Devices containing a CdSe quantum dot film . . . . .	60
4.3	Summary . . . . .	63
<b>5</b>	<b>Photocurrent spectra</b>	<b>65</b>
5.1	Measurement apparatus . . . . .	65
5.1.1	Description of measurement . . . . .	66
5.1.2	Quantum Efficiency . . . . .	67
5.2	Experimental results . . . . .	68
5.2.1	Control device without a quantum dot layer . . . . .	68
5.2.2	Devices with a quantum dot layer . . . . .	70
5.3	Summary . . . . .	72



<b>6</b>	<b>Photocurrent-voltage characteristics</b>	<b>75</b>
6.1	Measurement apparatus . . . . .	75
6.1.1	Description of measurement . . . . .	76
6.2	Experimental results and discussion . . . . .	77
6.3	Summary . . . . .	81
<b>7</b>	<b>Conclusion</b>	<b>83</b>
<b>A</b>	<b>Procedure for patterning ITO-glass substrates</b>	<b>85</b>
A.1	Supplies . . . . .	85
A.2	Procedure . . . . .	86
<b>B</b>	<b>Procedure for cutting patterned ITO-glass using the dicing saw</b>	<b>89</b>
B.1	Supplies . . . . .	89
B.2	Procedure . . . . .	90
<b>C</b>	<b>Procedure for solgel deposition of TiO<sub>2</sub> films</b>	<b>93</b>
C.1	Hazards . . . . .	93
C.2	Supplies . . . . .	94
C.3	Procedure . . . . .	94
<b>D</b>	<b>Procedure for purification of organic materials</b>	<b>97</b>
D.1	Hazards . . . . .	98
D.2	Supplies . . . . .	98
D.3	Procedure . . . . .	98
<b>E</b>	<b>Procedure for measuring current-voltage characteristics under illumination</b>	<b>101</b>
E.1	Calibration . . . . .	101
E.2	Apparatus . . . . .	102
E.3	Procedure . . . . .	102

<b>F</b>	<b>Procedure for measuring photocurrent spectra</b>	<b>105</b>
F.1	Cautions . . . . .	105
F.2	Apparatus . . . . .	106
F.3	Procedure . . . . .	106

# List of Figures

1-1	Absorption spectra of CdSe nanocrystals measured at 10 K . . . . .	21
1-2	Diagram of conduction band of QWIP structure . . . . .	23
1-3	Idealized density of states for one band of a semiconductor structure of 3, 2, 1 and 0 dimensions . . . . .	24
1-4	Depiction of typical device structure used for CdSe/conjugated poly- mer blend photovoltaics. . . . .	25
2-1	Energy band diagram in forward bias and reverse bias for a p-n junction.	28
2-2	Equivalent circuit model of an ideal diode with parasitic resistance. Also shown are current-voltage characteristics illustrating the limiting cases of infinite shunt resistance $R_{sh}$ and zero series resistance $R_s$ . . .	31
2-3	Schematic of dye-sensitized solar cell. . . . .	35
2-4	Schematic of CdSe system with molecular structure of TOPO and en- ergy level diagram. . . . .	37
2-5	Illustration of molecular orbitals in benzene (a) and chemical structure in explicit form (b) and condensed form (c). . . . .	38
2-6	Molecular structure of TPD. . . . .	39
2-7	Idealized pin heterojunction energy band diagram with bias dependence	41
2-8	Energy level alignment in our device. . . . .	42
3-1	TiO <sub>2</sub> thin film deposition process via sol-gel and AFM image of the surface of the resulting film. . . . .	44
3-2	Schematic diagram of RF-powered sputter deposition system. . . . .	45
3-3	AFM image of a sputtered TiO <sub>2</sub> film. . . . .	46

3-4	Diagram of thermal gradient sublimation system used to purify small molecule organic powders. . . . .	48
3-5	Diagram of colloidal CdSe quantum dot photodetector device. . . . .	49
3-6	Drawings of the probe fixture used to test photodetectors on half-inch substrates. . . . .	51
3-7	Electrodes and active layers of the device are patterned in order to make contact with gold pins from our probe fixture. . . . .	52
4-1	Diagram of setup for current-voltage measurements taken in ambient atmosphere. . . . .	54
4-2	Diagram of setup for current-voltage measurements taken in a nitrogen-filled glove box. . . . .	55
4-3	Diagram of electrical hook-up polarity . . . . .	56
4-4	Log-linear i-v characteristics and linear i-v characteristics of a device consisting of a TiO <sub>2</sub> layer spun via sol-gel and a spun TPD layer . . .	58
4-5	Log-linear i-v characteristics and linear i-v characteristics of a device consisting of a sputtered TiO <sub>2</sub> layer and an evaporated TPD layer. At low voltages shown here, the device displays low dark current (black line) and current saturation under illumination (red line). . . . .	59
4-6	Log-linear i-v characteristics of the same TiO <sub>2</sub> /TPD device before and after application of 0.5 V of reverse bias . . . . .	60
4-7	Log-linear i-v characteristics and linear i-v characteristics of a CdSe device measured under nitrogen . . . . .	61
4-8	Log-linear i-v characteristics and linear i-v characteristics of a treated CdSe device measured under nitrogen . . . . .	62
4-9	Current-voltage characteristics of a CdSe/TPD bi-layer device displays neither rectification nor sensitivity to light. . . . .	63
5-1	Diagram of setup used to measure photocurrent spectra (a) and illustration of incident beam spot size on a pad of the sample device (b). . . . .	66

5-2	Quantum efficiency % versus incident photon energy in eV of an ITO/TiO <sub>2</sub> /TPD/Ag device without a quantum dot layer . . . . .	69
5-3	Absorption spectrum (a) of an 80 nm CdSe film. The quantum efficiency % (b) of our ITO/TiO <sub>2</sub> /CdSe/TPD/Ag device is weak but measurable. The resulting internal quantum efficiency is low (c). . . . .	71
5-4	Absorption spectrum (a) of a 40 nm treated CdSe film. The quantum efficiency % of an ITO/TiO <sub>2</sub> /CdSe/TPD/Ag device with treated CdSe is significantly higher than that of the previously untreated device. The corresponding internal quantum efficiency (c) is relatively even across the CdSe absorption. . . . .	73
6-1	Diagram of setup used to measure photocurrent-voltage characteristics.	76
6-2	Response % of the ITO/TiO <sub>2</sub> /CdSe/TPD/Ag treated device, illuminated at 450 nm and 550 nm. . . . .	77
6-3	Scanning to higher voltages reveals saturation of the photocurrent response %. Illumination is at 550 nm. Both hysteresis and noise due to device instability at higher voltages are apparent. . . . .	78
6-4	Response % versus voltage of an ITO/TiO <sub>2</sub> /TPD/Ag device without a quantum dot layer. The sweep was repeated several times with no degradation. . . . .	80
6-5	Response % at 360 nm shows saturation, hysteresis and signal degradation between sweeps. . . . .	80
E-1	DC power supply rear panel connections and settings . . . . .	103
E-2	Front panel of “ivmeasure6.vi” . . . . .	103
E-3	Data is displayed in a new window . . . . .	104
F-1	LabView program “gotowavers232.vi” is used to set the wavelength of the monochromator . . . . .	107
F-2	LabView program “photocurrlockin3.vi” is used to measure the photocurrent spectrum . . . . .	108



# Chapter 1

## Introduction

A photodetector is an electronic device that converts incident photons into electric current. Photodetectors have a wide range of scientific and consumer applications and have played a central role in the development of modern physics during the last century. This thesis explores the possibility of fabricating a photodetector based on a relatively new material genre – colloidally grown quantum dots.

One of the broad hopes of colloidal quantum dot technology is to be able to create optoelectronic devices with all of the special properties inherent to inorganic semiconductors, yet be free of some of the constraints such as epitaxial lattice matching and small substrate size. Indeed, substantial progress has been made in incorporating quantum dots into organic light emitting diodes [1] and conjugated polymer photovoltaics [2]. However, there remain many steps and innovations necessary to make this technology a reality. In this work, we demonstrate a novel photodetector architecture which utilizes a pristine film of colloidal quantum dots as the primary photo-active component.

We begin this introductory section with some background information about quantum confinement, colloidal quantum dot technology and the principles of photodetection in general. From there, we explain the potential benefits of quantum dot photodetectors, including the prospect of more flexible material deposition processes and enhanced performance.

## 1.1 Introduction to photodetectors

Photodetectors have been used since the early 1900's in industry and scientific laboratories to measure light intensity. The earliest application was a light meter for photography, which used selenium (Se) as the light sensitive material. In 1873, Willoughby Smith was the first to discover photoconductivity when his experiments into the resistivity of selenium slabs were confounded by the fact that the resistivity changed under different lighting conditions [3]. Today, photodetectors are often comprised of a junction between p-type and n-type silicon – a *p-n junction*, discovered accidentally by Russel Ohl at Bell Labs in 1940 [4]. Photodetectors are now ubiquitous in both research and consumer applications, with the highest profile example being charge coupled device (CCD) arrays found in modern imaging devices like digital cameras.

Photodetectors can be made to be sensitive across a wide range of the electromagnetic spectrum, depending on the band gap of the absorbing material. Infrared sensitive photodetectors, for example, are often made of mercury cadmium telluride (HgCdTe), whose band gap ( $E_g$ ) varies from 0.2 eV to 0.1 eV, depending on the concentration of each constituent. UV photodetectors can be made out of silicon carbide (SiC) ( $E_g = 3$  eV) or even diamond ( $E_g = 5.47$  eV). Visible photodetectors are commonly made out of silicon (Si) ( $E_g = 1.12$  eV) [5].

### 1.1.1 Photodetector performance

Photodetectors are characterized in a number of ways, usually depending on the application. The most fundamental metric of photodetector performance is *quantum efficiency*  $\eta$ , which is the number of generated electrons per incident photon. In applications where light intensity is being measured, the most useful metric is *responsivity*  $R$ , which is the ratio of current per optical power. In applications where the signal to noise ratio is important, the main metric is the *detectivity*  $D^*$ . These metrics are described below in detail.



## Quantum efficiency $\eta$

Neglecting reflection, the quantum efficiency is given by

$$\eta = \zeta (1 - e^{-\alpha d})$$

where  $\zeta$  is the fraction of generated charge extracted from the device,  $\alpha$  is the absorption coefficient and  $d$  is the thickness of the device. Generally  $\eta$  is measured at zero bias, where only photogenerated charge contributes to photocurrent. P-n junction photodiodes with anti-reflection coatings often have quantum efficiencies greater than 90%.

## Responsivity $R$

Often photodetectors are strongly reverse biased in order to reduce response times. Under bias, generated charge can be reduced or amplified. In avalanche photodetectors (APDs), for example, charge is multiplied by impact ionization. This loss or amplification is called gain  $g$  and can vary anywhere from a small fraction to greater than  $10^4$ . A useful metric that incorporates gain is the responsivity – the amount of electrical current  $I$  flowing per incident optical power  $P$ . The responsivity  $R$  is given by

$$R = \frac{I}{P} = \eta q g \frac{\lambda}{hc}$$

where  $q$  is the charge of an electron,  $\lambda$  is the wavelength of incident light,  $h$  is Planck's constant and  $c$  is the speed of light.  $R$  is often used to characterize visible wavelength photodetectors. A typical value of  $R$  for a silicon photodiode is 0.4 A/W at  $\lambda = 600$  nm. Gain  $g$  in a silicon photodiode is usually close to one.

## Background noise current

In the infrared, background radiation can overwhelm the original signal so it is important to consider the effect of noise current. Generation of carriers in bulk semiconductors is instigated by both thermal radiation and optical radiation. Thermal radiation

originates from blackbody emission of the semiconductor device itself, which always has a finite temperature. Optical radiation comes from photons in the imaging field that are not due to the signal. The total generation rate  $G$  is equal to

$$G = \frac{dn}{dt}$$

where  $n$  is the number of generated electrons per unit volume of the semiconductor. These electrons have an associated charge  $Q$  equal to

$$Q = nqgA_e d$$

where  $q$  is the charge of an electron,  $g$  is the gain,  $d$  is the thickness of the light absorbing film and  $A_e$  is the electrical area of the device. These generated carriers can support a generation current  $I_G$ , which is

$$I_G = \frac{dQ}{dt} = \frac{d}{dt}(nqgA_e d) = qgA_e d \frac{d}{dt}n = qgA_e dG.$$

Some of the generated carriers will recombine before being able to contribute to current flow. Carriers that recombine will create an opposing recombination current  $I_R$  that follows the same functional form as  $I_G$ :

$$I_R = -qgA_e dR$$

The generation of carriers is random and therefore follows the rules of Poisson counting statistics. The probability of obtaining  $r$  number of carriers over a time interval  $\tau$  is given by

$$P_r = \frac{N^r}{r!} e^{-N}$$

where  $N$  is the expected number of carriers counted during time  $\tau$  and is given by

$$N = A_e dG\tau.$$

The accuracy with which the value of  $N$  can be determined is given by  $\sigma$ , the square root of the variance

$$\sigma = \sqrt{N} = \sqrt{A_e d G \tau}.$$

The time  $\tau$  taken to count the number of generated carriers sets a limit on the detectable frequency bandwidth  $\Delta f$  according to the *Nyquist sampling theorem*:

$$\tau = \frac{1}{2\Delta f}.$$

The background current  $I_G$ , measured over the time interval  $\tau$ , is then known to within an accuracy of  $\pm I_n$ , where  $I_n$  is the noise current, written as [6]

$$I_n = qg \frac{\sigma}{\tau} = qg \frac{\sqrt{A_e d G \tau}}{\tau} = qg \sqrt{\frac{A_e d G}{\tau}} = qg \sqrt{A_e d G 2\Delta f}.$$

The same logic applies to the recombination current  $I_R$ . We obtain the total noise current by adding the contribution from generation and recombination in quadrature, resulting in:

$$I_n = qg \sqrt{A_e d (G + R) 2\Delta f}.$$

### **Detectivity, $D^*$**

A common way to incorporate the responsivity  $R$  and noise current  $I_n$  into a single metric is with the detectivity  $D^*$ , defined as

$$D^* = R \frac{\sqrt{A_o \Delta f}}{I_n}$$

where  $A_o$  is the optically active area and  $\Delta f$  is the bandwidth. Combining the above equations for  $R$  and  $I_n$ , we can reduce the expression for  $D^*$  to

$$D^* = \eta \frac{\lambda}{hc} \frac{1}{\sqrt{2(G + R)d}} \sqrt{\frac{A_o}{A_e}}$$

The thickness  $d$  of a device is chosen in order to maximize absorption while mini-

mizing generation and recombination losses. It can be shown that setting the device thickness to

$$d = \frac{1.26}{\alpha}$$

where  $\alpha$  is the absorption coefficient, results in the best signal to noise ratio [7].

Using the fact that  $t \propto 1/\alpha$ , we can see the major dependencies of  $D^*$  by fixing  $t$  and noticing that  $\eta \propto \zeta$

$$D^* \propto \zeta \frac{\lambda}{hc} \sqrt{\frac{\alpha}{(G + R)}}$$

$$D^* \propto \zeta \frac{\lambda}{hc} \sqrt{\frac{\alpha}{G}}$$

where we've used the fact that  $G = R$  in equilibrium. The figures of merit are then  $\zeta$  and  $(\alpha/G)$ , meaning that high quantum efficiency should be combined with high absorption. Absorption is important because of its inverse relationship to thickness. With greater thickness, there is more material volume to contribute toward unwanted generation and recombination events, which increase  $I_n$  and degrade performance. To raise  $D^*$ , one must increase  $(\alpha/G)$ .

## 1.2 Low-dimensional semiconductors

A semiconducting structure that limits the motion of charge carriers to two, one or zero dimensions is often referred to as a low-dimensional semiconductor. For example, an ultra-thin film allows charge to propagate in the x and y directions, but not in the z direction, resulting in what's called a two-dimensional semiconductor. A zero-dimensional semiconductor constrains an electron in all three dimensions and is often called a quantum dot [8].

Since the early 1980's, low-dimensional semiconductors have appeared in optoelectronic devices such as photodetectors [9], lasers [10] and optical modulators. Their unique optical and electronic properties stem from the physical phenomenon called quantum confinement, which occurs when a semiconductor's dimensions approach the

de Broglie wavelength of an electron:

$$\lambda = \frac{h}{p}$$

where  $h$  is Planck's constant and  $p$  is the electron momentum. With decreasing thickness, the semiconductor's broad energy level bands collapse into discrete energy levels  $E_n$  that can be approximated by assuming an infinite square potential well, as in the textbook one dimensional quantum mechanics problem. The energy levels are given by

$$E_n = \frac{\hbar^2}{2m^*} \left( \frac{n\pi}{L_z} \right)^2$$

where  $\hbar = h/2\pi$ ,  $m^*$  is the electron effective mass,  $L_z$  is the size of the quantum well and  $n$  is an integer. These discrete energy levels can be tuned by changing the width of the well without changing the materials themselves.

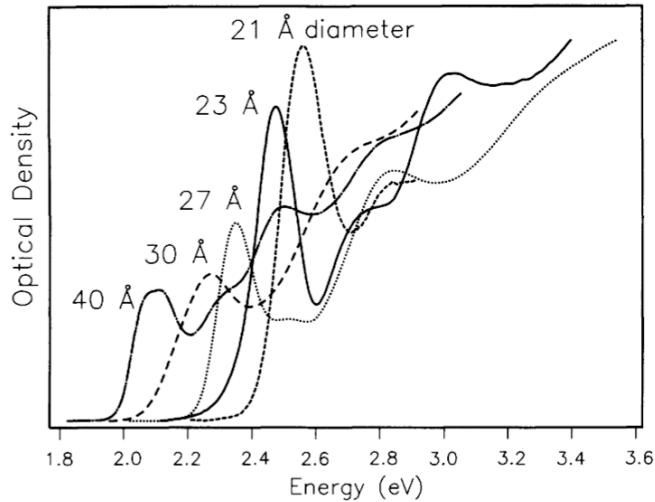


Figure 1-1: Absorption spectra of CdSe nanocrystals measured at 10 K. Spectra have been scaled for clarity. From D. M. Mittleman [11].

Modification of the electronic state density and narrow emission from transitions between discrete states have enabled quantum well laser diodes [10]. Quantum wells also exhibit special electronic properties like enhanced electron impact ionization, as seen in low-noise avalanche photodetectors [12]. An important consequence of

confinement for photodetectors is the increase in the absorption coefficient (Figure 1-1). One way to understand this increase is to consider that the same material volume, unconfined, will experience a similar number of absorption events as the confined volume. The unconfined volume will absorb across a broad range of wavelengths and the confined volume will absorb only at discrete wavelengths, but with greater probability.

### 1.2.1 Quantum well infrared photodetectors

Many inorganic photodetectors operate at near infrared ( $\lambda = 0.7$  to  $3 \mu\text{m}$ ) and middle infrared ( $\lambda = 3$  to  $5 \mu\text{m}$ ) wavelengths – a range important for applications like infrared imaging and automotive sensors. Quantum well infrared photodetectors (QWIPs) use layered heterostructures of two lattice-matched semiconductors with a significant energy level offset. By sandwiching a high electron affinity semiconductor (the well material) between a low electron affinity semiconductor (the barrier material) and by limiting the thickness of the high electron affinity layer, one can form discrete energy levels in the resulting electron well. Transition energies between bound states or bound and unbound states in the well can be in the infrared wavelength range and can generate photocurrent when excited by an infrared photon [9].

Usually quantum well devices are grown as multi-layered superlattice structures. Epitaxial deposition techniques such as molecular beam epitaxy (MBE) are required to achieve precise thickness control and defect-free lattice-matched layer interfaces [13]. These growth constraints tend to limit the substrate size and the available set of materials because few material combinations exist that have both a large band gap offset and minimal change in their lattice constant. The GaAs/AlGaAs material system is the most widely used. GaAs substrates are generally limited to 6 inches in diameter.

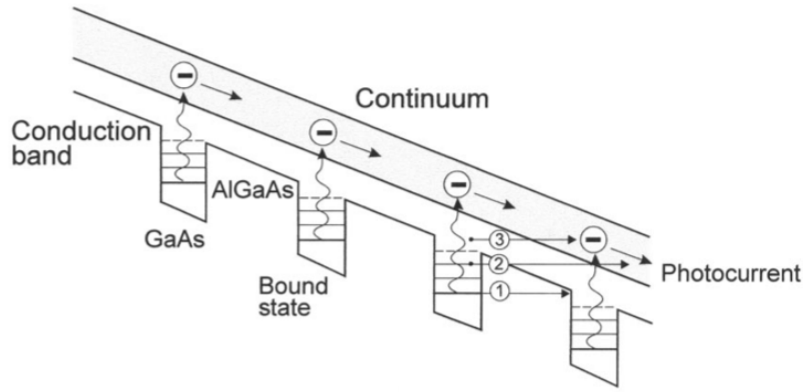


Figure 1-2: Diagram of conduction band of QWIP structure. Photocurrent is generated when a bound state electron in a well is excited into the continuum. Three mechanisms that create dark current are shown: (1) ground state sequential tunneling, (2) intermediate thermally assisted tunneling and (3) thermionic emission. From A. Rogalski [7].

### 1.2.2 Quantum dot infrared photodetectors

To improve on the performance of QWIPs, researchers have built quantum dot infrared photodetectors (QDIPs) that are based on epitaxially grown three dimensional islands. The QDIP was first proposed in 1996 by V. Ryzhii [9]. Because of the additional plane of confinement, the density of states increases and the profile becomes a delta function, in contrast to the step function density of states of 2D quantum wells, as shown in Figure 1-3. The peaked density of states leads to better absorption, narrow band detection and a smaller thermal generation rate. In QDIPs, the quantum dots are formed by the Stranski-Krastanov (SK) process where a thin layer of material is deposited onto a substrate with a much smaller lattice constant. The strain between the two layers causes nucleation of randomly distributed, but evenly shaped and sized quantum dots. Generally, the shape of the dots tends to be pyramidal. The most common QDIP material system is the InAs/GaAs heterostructure. Quantum efficiencies for quantum well infrared photodetectors (QWIPs) are generally less than 10% because of low absorption and poor charge extraction [9].

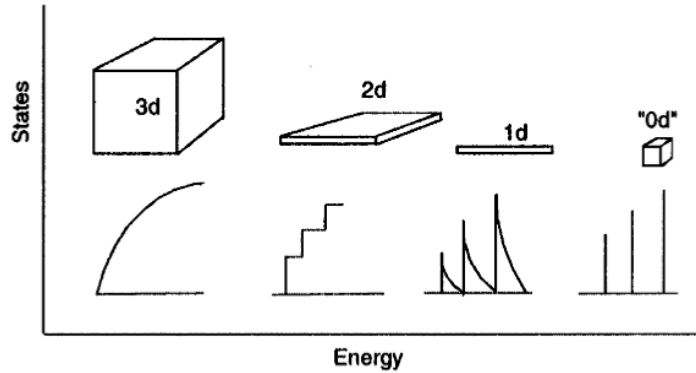


Figure 1-3: Idealized density of states for one band of a semiconductor structure of 3, 2, 1 and 0 dimensions. From Alivisatos [14].

## 1.3 Colloidal quantum dot technology

Colloidal quantum dot technology arose in the early 1980's when scientists at both Bell Labs and in the former Soviet Union noticed that solutions of semiconductor nanoparticles were colored differently although the semiconductor material was the same [15]. Since then, high purity semiconductor nanocrystals have been grown synthetically and processed with organic capping groups so that they can be deposited from organic solutions [16].

Solution processable colloidal quantum dot systems display many of the special optical and electronic properties associated with epitaxially grown quantum confined systems [14]. Their tunable band gap and their higher absorption relative to the bulk make quantum dots particularly attractive as photogeneration materials. At the same time, colloidal quantum dots offer much greater material system flexibility than epitaxial quantum dots because deposition on any substrate is possible [1]. This flexibility is central to our work because it allows us to independently choose a substrate and a top contact layer that are optically transparent and electrically compatible.

### 1.3.1 Colloidal quantum dot photodetectors

A photovoltaic effect in quantum dot/conjugated polymer blends was first observed by Greenham, et al. [17]. In these devices, CdSe quantum dots are used as both an



absorber and electron acceptor. The efficiency was found to be limited in part by poor transport through the network of quantum dots [18]. Larger efficiencies have been reported using CdSe nanorods, in which transport is improved along the extent of the rods [19] [2]. However, resistive losses remain an issue because the nanorods tend to lay flat, perpendicular to the direction of current flow [20]. Sun, et al. [21] have achieved a quantum efficiency of 15% at the quantum dot absorption edge using branched CdSe tetrapods comprised of four limbs connected at a central core. Their device structure consists of a CdSe tetrapod/conjugated polymer composite film (86% Cdse by weight) spun onto a PEDOT film and covered with aluminum as the top electrode, as shown in Figure 1-4.

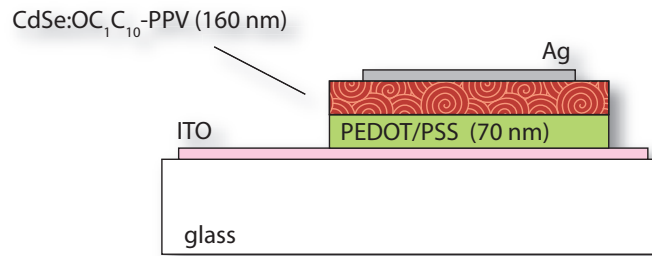


Figure 1-4: Depiction of typical device structure used for CdSe/conjugated polymer blend photovoltaics.

So far, colloidal quantum dot detectors make use of transitions from electron states in the valence band to the conduction band, unlike epitaxial GaAs quantum well and quantum dot infrared detectors which rely on transitions within states in the conduction band, as described in section 1.2.1. The absorption coefficient  $\alpha$  of intersubband transitions is low (less than  $10^3 \text{ cm}^{-1}$ ), whereas  $\alpha$  for direct band transitions is usually greater than  $10^4 \text{ cm}^{-1}$ . For this reason, direct band to band infrared detectors like mercury cadmium telluride (HgCdTe) have higher detectivities than QWIPs. It may be possible to use colloidal quantum dot technology to fabricate large area lead sulfide (PbS) or even HgCdTe infrared detectors.

## 1.4 Our device concept

Our goal is to fabricate a device structure that will both function as a photodiode and facilitate measurement of photoconduction in CdSe quantum dot films. Devices consisting of a single quantum dot film are rare [22] because it is difficult to deposit a uniform film of pure quantum dots. Lateral photoconductor geometries, however, have been used successfully to measure transport and photoconductivity [23].

Our solution is to insert a colloidal quantum dot film into the middle of a bilayer device that already functions as a rectified diode. In this way, mechanical gaps in the quantum dot film will not cause the overall device to be shunted. The bilayer device that we have chosen is a metal-oxide/organic semiconductor heterostructure that has already been used in organic small molecule photovoltaics [24] [25].

## 1.5 Structure of thesis

In Chapter 2, we begin with a brief description of each material used in our multi-layered photodetector device. We give an introduction to the basic device physics needed to understand photocurrent generation and then discuss the rationale behind our particular material system. The fabrication processes and equipment are described in Chapter 3. Chapters 4 and 5 describe the measurement of current-voltage characteristics and photocurrent spectra. The results show good diode behavior and modest light sensitivity. In the final chapter, Chapter 6, we describe the measurement of photocurrent under bias. This data gives evidence for high hole trap densities in the quantum dot film and affirms one of our initial design goals – that of blocking charge injection in reverse bias.

# Chapter 2

## Theoretical background and photodetector design considerations

In the introductory chapter, we described the potential benefits of a colloidal quantum dot system, with its peaked density of states, simple device manufacturability and potentially low dark current. In this chapter, we will describe the device architecture used in our quantum dot photodetector design and the essential theoretical background needed to understand device operation. Our material set draws from an ordinarily disparate set of semiconductor technologies. We attempt to capitalize on the hardness and chemical stability of metal oxide semiconductors, on the solution processability of quantum dots and on the ability of organic semiconductors to be deposited from the vapor phase.

### 2.1 Ideal p-n junction diode

As background, we will briefly review the basic theory behind the p-n junction and the equivalent circuit model of a photodiode. Note that the physics of junctions between crystalline semiconductors is fundamentally different than that of junctions between low-mobility amorphous-crystalline semiconductors – the materials which are used in

this work. However, the idealized device model applies reasonably well and is useful in understanding the current-voltage characteristics.

### 2.1.1 Description of the p-n junction

William Shockley was the first to describe the physical behavior of the p-n junction in 1948. He introduced the notion of minority carriers to explain why opposite charge can briefly co-exist side by side in a semiconductor. Below, we discuss how minority carrier injection and extraction across a p-n junction leads to rectified behavior.

The junction between a p-type semiconductor in contact with an n-type semiconductor results in the formation of a depletion region. Higher energy electrons, which are plentiful in the n-type layer, lower their energy by transfer to the p-type layer. Likewise higher energy holes in the p-type region transfer to the n-type layer. In the steady state, this transfer of charge leaves a small region at the junction that is completely devoid of free carriers and is occupied only by the remaining fixed charge due to ionized dopants in the semiconductor lattice. Over the whole device, charge neutrality is maintained. Ionized donor molecules in the n-region are positively charged and ionized acceptor molecules in the p-region are negatively charged. The fixed charge causes an electric field across the junction which is determined by the density of dopants in each layer. It is important to note that the electric field exists even though there is no external bias applied across the junction.

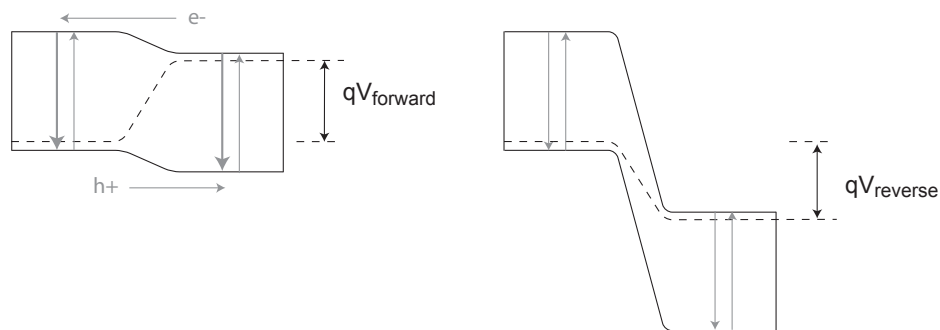


Figure 2-1: Energy band diagram in forward bias and reverse bias for a p-n junction.

Under forward bias (Figure 2-1), the equilibrium is upset and more electrons from the n-type layer are fed across the depletion region over into the p-type layer. An injected electron, now a minority carrier, can diffuse through the conduction band of the p-type layer for a short while (given by the carrier lifetime  $\tau_e$ ) and eventually recombine with a hole. For an electron, the average diffusion distance is the diffusion length  $L_e$ , given by

$$L_e = \sqrt{D_e \tau_e}$$

where  $D_e$  is the electron diffusion constant. Once electrons have successfully crossed the junction and recombined in the p-region, the process of current flow through the device is effectively complete, assuming efficient exchange of carriers at the Ohmic electrodes. The magnitude of the current density due to electron injection  $J_e$  depends on the net rate of recombination  $R$ :

$$J_e = \frac{d\rho}{dt} = L_e \frac{dQ}{dt} = qL_e \frac{dn}{dt} = qL_e R$$

where  $\rho$  is charge per area,  $Q$  is charge per volume,  $q$  is the charge of an electron and  $n$  is the number of electrons per volume. The recombination rate varies according to the number of injected minority carriers  $n$ :

$$R = \frac{D_e}{L_e^2} n = \frac{1}{\tau_e} n.$$

The concentration of carriers spilling over the interface into the p-type layer must be equal to the concentration of majority carriers in the n-type layer that have energies greater than the energy level of the conduction band of the p-region (see Figure 2-1). The distribution in energy of electron states in the conduction band can be approximated by assuming Boltzmann statistics, where the number of carriers in the conduction band is given by:

$$n \simeq N_c \exp \frac{E_F - E_c}{kT}$$

where  $N_c$  is the effective density of states of the conduction band,  $E_F$  is the Fermi level and  $E_c$  is the conduction band energy level. We can rewrite this equation in terms of the voltage applied across the p-n junction if we assume that the injection regime is not far from equilibrium:

$$n \simeq \frac{n_i^2}{N_A} \exp \frac{qV}{kT}$$

where  $n_i$  is the intrinsic carrier concentration,  $N_A$  is the acceptor concentration in the p-region and  $V$  is the voltage applied across the junction. As a final correction, we subtract the equilibrium electron concentration in the p-region because recombination from these carriers is offset by equilibrium thermal generation:

$$n = \frac{n_i^2}{N_A} \left( \exp \frac{qV}{kT} - 1 \right)$$

The electron current density is then:

$$J_e = q \frac{D_e}{L_e} \frac{n_i^2}{N_A} \left( \exp \frac{qV}{kT} - 1 \right).$$

Following the same logic for hole extraction from the p-region to the n-region, we obtain the total current density:

$$J = J_e + J_h = q \left( \frac{D_e}{L_e} \frac{n_i^2}{N_A} + \frac{D_h}{L_h} \frac{n_i^2}{N_D} \right) \left( \exp \frac{qV}{kT} - 1 \right) = J_s \left( \exp \frac{qV}{kT} - 1 \right)$$

where  $J_h$  is the hole current density,  $D_h$  is the hole diffusion constant in the n-region,  $L_h$  is the hole diffusion length,  $N_D$  is the donor dopant density of the n-region and  $J_s$  is the saturation current density.

### 2.1.2 Equivalent circuit model under illumination

When light is incident on a p-n junction, electron and hole carriers are produced throughout the film. Minority electrons generated in the p-region can diffuse across the junction to the n-region in order to contribute toward photocurrent. Minority

holes generated in the n-region can diffuse over to the p-region and contribute to photocurrent. The total photocurrent is flowing in parallel with the ordinary diode processes described in the previous section and can be modeled as shown in Figure 2-2. The parasitic series resistance  $R_s$  is the resistance experienced by photogenerated carriers as they travel to the electrodes.  $R_s$  should be as close to zero as possible otherwise photocurrent at high intensities becomes subject to resistive losses. The parasitic shunt resistance  $R_{sh}$  is due to leakage pathways that bypass the junction.  $R_{sh}$  should be large otherwise it will lead to poor rectification. The diode equation under illumination including parasitic resistances becomes:

$$J = J_{sc} - J_s \left( \exp \left\{ \frac{qV}{kT} + \frac{qJAR_s}{kT} \right\} - 1 \right) - \frac{V + JAR_s}{R_{sh}}$$

where  $J_{sc}$  is the short circuit current density under illumination and  $A$  is the area of the device.

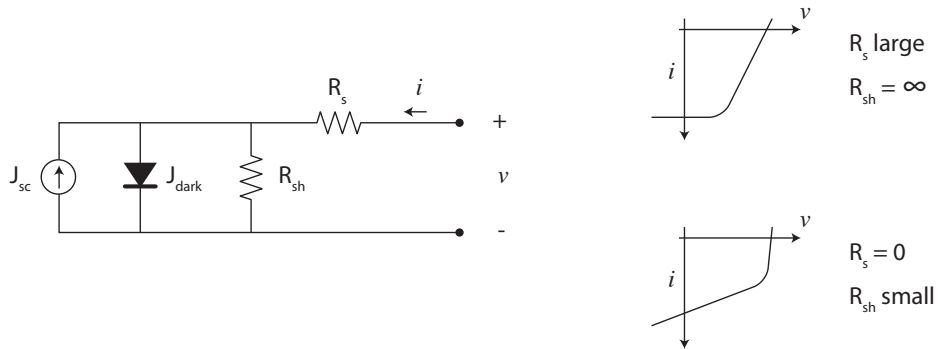


Figure 2-2: Equivalent circuit model of an ideal diode with parasitic resistance. Also shown are current-voltage characteristics illustrating the limiting cases of infinite shunt resistance  $R_{sh}$  and zero series resistance  $R_s$ .

## 2.2 Semiconducting metal oxides

One generally thinks of oxides as being insulating. Silicon dioxide ( $\text{SiO}_2$ ), for example, plays an important role as an insulator in field effect transistors. However,

metal oxides have been known to be semiconducting ever since the first Schottky junction was discovered in 1926, when Grondahl and Geiger fabricated a cuprous oxide (CuO)/copper diode. In fact, many as-grown metal oxide films naturally exhibit semiconducting behavior, most notably zinc oxide (ZnO) and titanium dioxide (TiO<sub>2</sub>). Current knowledge of oxide semiconductors is relatively limited, mainly due to technological difficulties in growing high purity single crystals and the more complex structure of oxides compared to elemental semiconductors. As-grown oxide films tend to deviate from stoichiometry, leaving oxygen vacancies that cause modest n-type doping, although some oxides like CuO and nickel oxide (NiO) have metal atom vacancies and hence p-type character. The concentration of defects depends on growth conditions like pressure, temperature and the presence of oxygen. By virtue of the strong ionic bonds that hold oxide molecules together, oxides tend to have large band gaps, often greater than 3 eV [26].

Because single crystal growth is difficult, oxide films are commonly amorphous-crystalline, with grain sizes on the order of tens of nanometers. Compared to single crystalline semiconductors, amorphous semiconductors have lower mobilities resulting from reduced long-range order and increased trap densities due to dangling bonds and lattice defects. In inorganic crystalline semiconductors, conduction is typically Ohmic:

$$J = \sigma E = qn\mu dV$$

where  $J$  is the current density,  $\sigma$  is the conductivity,  $E$  is the electric field,  $q$  is the charge of an electron,  $n$  is the number of carriers,  $\mu$  is the mobility,  $d$  is the thickness and  $V$  is the voltage. The mobility is influenced primarily by scattering from phonons and dopant impurities. The temperature dependence of the mobility can be approximated by [27]

$$\mu \propto (m^*)^{-3/2} T^{1/2}$$

where  $m^*$  is the electron effective mass and  $T$  is the temperature. In some metal oxides, band-like transport has been observed, although with heavy electron effective masses (on the order of 1x to 10x the mass of an electron, compared to  $\sim 0.1x$  for



typical semiconductors), indicating narrow energy bands due to limited wavefunction overlap between neighboring molecules. In other metal oxides, very narrow bands or even completely localized energy levels exist. In these cases, conduction follows a thermally activated hopping mechanism, with mobility given by

$$\mu \propto \exp -\frac{E_t}{kT}$$

where  $E_t$  is the activation energy of trapped carriers and  $k$  is Boltzmann's constant. The localized carrier and the polarization it induces in its surroundings is called a polaron. Charge transport occurs via tunneling between localized polaron states. In low mobility semiconductors that are devoid of free carriers, charge must be injected from an electrode into the bulk in order for conduction to take place. Charge build up near the injecting electrode usually results in *space charge limited current*, given by

$$J = \frac{9}{8} \epsilon \mu \frac{V^2}{d^3}$$

where  $\epsilon$  is the dielectric constant,  $\mu$  is the mobility and  $d$  is the film thickness. In materials with large trap densities, conduction is *trap limited*:

$$J \propto \mu \frac{V^{\frac{E_t}{kT}+1}}{d^{\frac{2E_t}{kT}+1}}$$

### 2.2.1 Electron-accepting TiO<sub>2</sub>

One of the most common oxides is titanium dioxide (TiO<sub>2</sub>). Titanium is an abundant element, accounting for about 0.6% of the earth's crust by weight and occurs in nature predominantly in the form of ilmenite, which is an ore containing iron, titanium and oxygen. Ilmenite can be upgraded to TiO<sub>2</sub> by a synthetic process that removes the iron. One of the most important uses of TiO<sub>2</sub> is as a white pigment, often used in paints, plastic, paper, ink, food and toothpaste. TiO<sub>2</sub> has a high refractive index (n=2.4) and a wide band gap ( $E_g=3.0 - 3.2$  eV), making it an effective scatterer at all wavelengths of visible light. TiO<sub>2</sub> is also an important photocatalytic material

for decomposing organic compounds. Under ultra-violet light, an electron hole pair is created and the resulting free-radicals can oxidize organic matter. The photocatalytic activity of  $\text{TiO}_2$  is useful in water treatment systems, air purification systems and antimicrobial coatings. The UV-resistance, chemical stability and mechanical hardness of  $\text{TiO}_2$  thin films is useful for automotive and building material coatings.

The crystal structure of  $\text{TiO}_2$  assumes three forms: rutile, anatase or brookite. The rutile phase is the most common, but for device applications anatase is more desirable because its lattice structure is denser, yielding greater overlap between molecular orbitals and hence higher mobilities. Hall-effect measurements of sputtered anatase films give electron mobilities as high as  $20 \text{ cm}^2/\text{Vs}$  [28] [29]. The band gap of anatase is 3.2 eV, slightly higher than that of rutile at 3.0 eV. Current-voltage measurements by Stamate [30] of  $\text{TiO}_2$  sandwiched between aluminum electrodes yield Ohmic conduction up to  $0.4 \text{ mA}/\text{cm}^2$ , space charge limited conduction between  $0.4 \text{ mA}/\text{cm}^2$  and  $1 \text{ mA}/\text{cm}^2$  and trap limited conduction above  $1 \text{ mA}/\text{cm}^2$ .

### 2.2.2 $\text{TiO}_2$ in photovoltaic devices

$\text{TiO}_2$  has been used for some time as an electron-accepting layer in dye-sensitized photovoltaics. In these devices, a  $10 \mu\text{m}$  nanoporous  $\text{TiO}_2$  film consisting of sintered  $\text{TiO}_2$  nanocrystals forms a high surface area substrate onto which strongly absorbing dye molecules can bind and inject electrons upon photo-excitation (Figure 2-3). Carrier concentrations in  $\text{TiO}_2$  are low, leading to high resistivities, but electrons injected into the conduction band are free carriers, able to traverse the film with minimal losses. The thick sensitized  $\text{TiO}_2$  film is submerged in a liquid electrolyte that serves to replenish electrons to the donor dye molecules, completing the circuit and allowing for the passage of current. Conversion efficiencies for the first device of this kind were reported to be 10% [31], but subsequent research has failed to improve on this number and the theoretical maximum efficiency has yet to be established.

For the bottom contact of our photodetector device, we are interested in a thin, smooth, dense and transparent n-type film.  $\text{TiO}_2$  satisfies these requirements. As opposed to organic semiconductors, metal oxides tend to be more stable and have

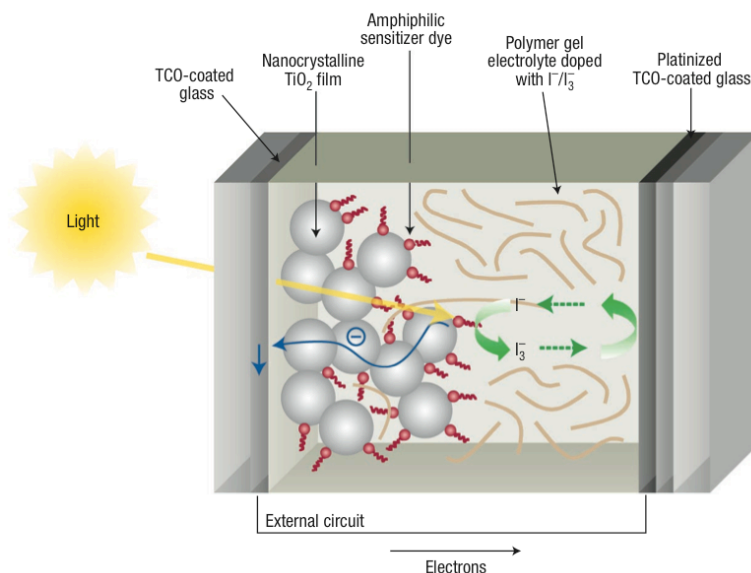


Figure 2-3: Schematic of dye-sensitized solar cell. From Durrant, et al. [32] [33].

higher mobilities. Their mechanical hardness and resistance to high temperatures allows solution deposition, annealing or chemical treatment of overlying quantum dot films.  $\text{TiO}_2$  can be deposited either by radio frequency (rf) sputtering or by spin coating from a sol gel precursor solution, although sputtering provides greater control over film thickness, morphology and doping concentration.

The challenge is that few reports have been published using sputter deposited metal oxide films in photodetector devices, so deposition parameters conducive to good working devices are largely unknown. Sol gel  $\text{TiO}_2$  films, on the other hand, have been widely used in conjunction with organic semiconductors [24, 25, 34, 35, 36, 37, 38, 39]. The advantage of sol gel layers is that they can be patterned with low-cost stamping [39] or micro-emulsion techniques [38]. Porous nanocrystalline  $\text{TiO}_2$  films have been sensitized by a wide range of quantum dots including lead sulfide (PbS) [40, 41, 42], cadmium telluride (CdTe) [43], indium phosphide (InP) [44], CdSe [45] and cadmium sulfide (CdS) [46, 47].

## 2.3 The CdSe quantum dot film

Cadmium selenide (CdSe) is an ionically bonded semiconductor with a direct band gap of 1.7 eV and an electron mobility of 800 cm<sup>2</sup>/Vs. CdSe crystals with perfect stoichiometry and crystal structure are insulating with low intrinsic carrier concentrations. In this work, CdSe nanocrystals are grown synthetically to a diameter of 4 nm. At this size, quantum confinement increases the band gap to 2.2 eV. During synthesis, the surface of the quantum dot is functionalized with the organic molecule trioctylphosphine oxide (TOPO). TOPO capping groups are transparent, insulating and extend about 1-2 nm beyond the nanocrystal surface (Figure 2-4). The resulting large interparticle spacing prohibits interparticle sharing of electron states and hence the mobility is reduced significantly. Ginger, et al. [48] have obtained low mobilities of 10<sup>-4</sup> to 10<sup>-6</sup> cm<sup>2</sup>/Vs from current-voltage characteristics fitted with a trap limited space charge conduction model, but mobility has not yet been measured directly. Annealing CdSe nanocrystal films reduces the interparticle spacing, with in turn increases the mobility [49]. Ridley, et al. [50] found relatively high field-effect electron mobilities of around 1 cm<sup>2</sup>/Vs in a transistor geometry where the CdSe film was synthesized without organic capping groups and sintered at 350C.

Jarosz, et al. [23] found that a butylamine treatment of CdSe quantum dot films resulted in enhanced photocurrent. It was shown that interparticle spacing decreases in treated samples. Also, butylamine is thought to passivate recombination centers at the quantum dot surface. In these experiments, Jarosz observed that the photocurrent reached saturation at 60 V applied across a 1 micron channel length (corresponding to an electric field of 6 x 10<sup>7</sup> V/m) and speculated that all photogenerated charge was being collected in the saturation limit. This conclusion assumes that charge cannot enter the device at the electrodes, otherwise photocurrent saturation could be attributed to some sort of dramatic increase in resistivity. One way to test the blocking contact hypothesis is to engineer a device with built-in blocking contacts and identify whether the photocurrent saturates at similar electric fields. We will return to this issue in section 2.5.1.

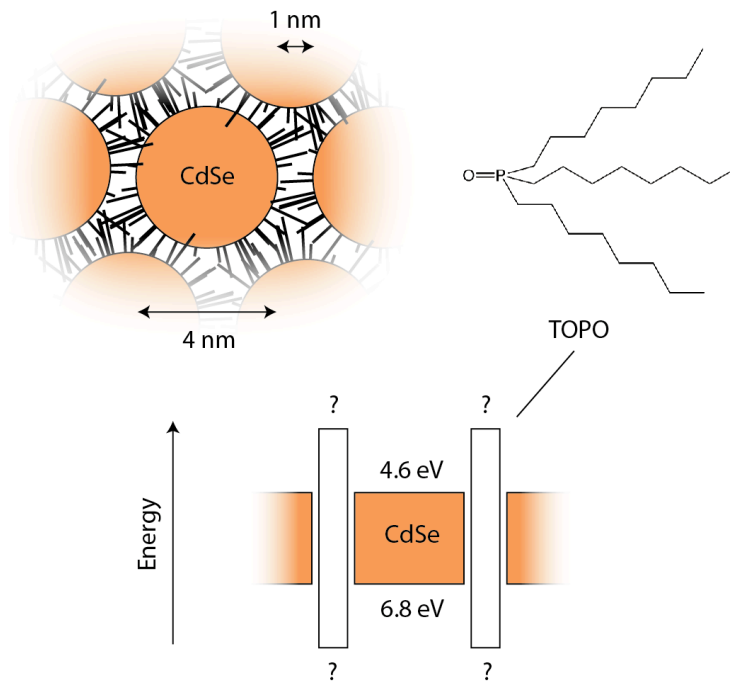


Figure 2-4: Schematic of CdSe system with molecular structure of TOPO and energy level diagram.

## 2.4 Organic semiconductors

An organic solid is a molecular material that contains carbon. Research into organic semiconductors began in 1906 when Pochettino discovered photoconductivity in solid anthracene. In the past twenty years, the field of organic semiconductors has expanded rapidly, driven largely by the prospect of new materials for light emission, light harvesting, lasing, superconductivity and molecular transistors. Organic molecular solids consist of covalently bonded molecules that are weakly bound to each other by van der Waals forces. They are characterized by low melting points, low conductivity, high absorption and soft structural properties. Organic molecules exhibiting semiconducting behavior are in a special class called conjugated aromatic hydrocarbons. Conjugation refers to the alternating sequence of single and double bonds, displayed for example by benzene (Figure 2-5), a ring of six hydrogen and six carbon atoms arranged in a hexagon. Such conjugation along chains of atoms often leads to

the ability to conduct charge due to the resonant sharing of electron across atoms.

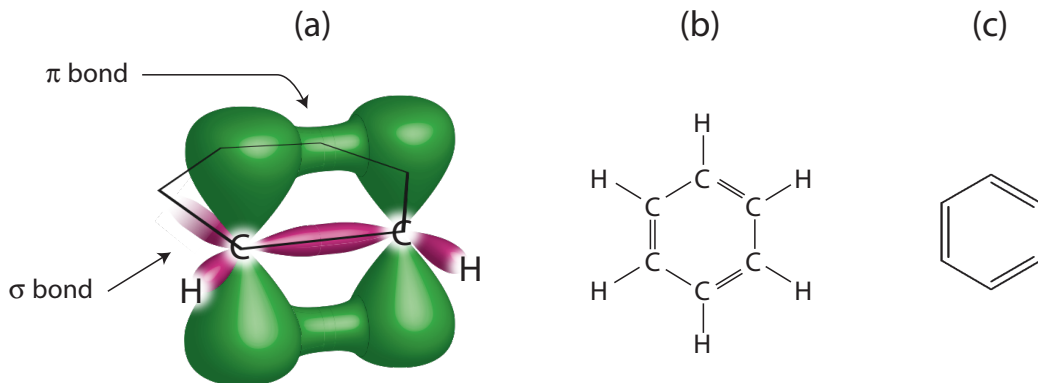


Figure 2-5: Illustration of molecular orbitals in benzene (a) and chemical structure in explicit form (b) and condensed form (c).

When a carbon atom is brought close to another carbon or hydrogen atom, the electron wavefunctions change their spatial configuration to accommodate the new potential energy situation. In the case of benzene, three electrons of the six total electrons on a carbon atom distribute themselves at roughly  $120^\circ$  increments in the plane of the molecule. These electrons form covalent bonds with other carbon or hydrogen atoms, called  $\sigma$  bonds. A fourth electron remains distributed in the  $z$  direction, above and below the plane of the molecule, and loosely binds to other  $z$ -distributed electrons from neighboring carbon atoms. These bonds are called  $\pi$  bonds and the resulting  $\pi$  electron system is delocalized over the entire benzene molecule.

Between molecules, van der Waals forces resulting from induced dipole-dipole interactions are responsible for intermolecular attraction. Electron delocalization is not present over intermolecular length scales, but some electron wavefunction overlap leads to the possibility of tunneling between molecules and ultimately charge conduction. Optical absorption occurs when the  $\pi$  electron - which is in the highest occupied molecular orbital (HOMO) - is excited to the next available unfilled state - the lowest unoccupied molecular orbital (LUMO). This excited electron state is called the  $\pi^*$  orbital. For each molecule,  $\pi$ - $\pi^*$  transitions occur at a well-defined energy level. But over the whole molecular solid,  $\pi$ - $\pi^*$  transition energies vary broadly because of

molecular deformations and local electric field variations due to intermolecular dipole interactions.

### 2.4.1 The organic hole transport molecule TPD

For the top, p-type contact to the CdSe film, we use the hole transporting organic small molecule N,N'-diphenyl-N,N'-bis(3-methylphenyl)-(1,1'-biphenyl)-4,4'-diamine (TPD), a common organic semiconductor used in electrophotography and organic LEDs. The TPD film is deposited by thermal evaporation on top the the CdSe film. The molecular structure of TPD is shown in Figure 2-6. Transport in TPD takes place via hopping of holes among TPD molecules, which occurs relatively efficiently, as reflected in it's mobility of  $10^{-3}\text{cm}^2/\text{Vs}$ .

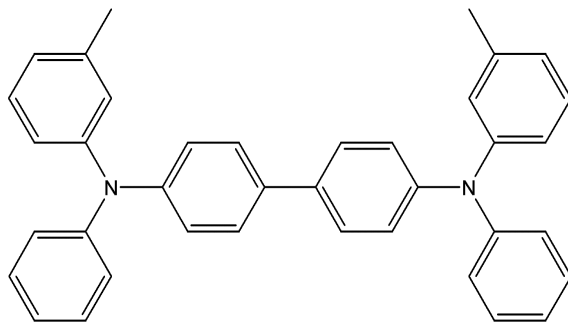


Figure 2-6: Molecular structure of TPD.

## 2.5 Our device architecture

Our proposed photodetector relies on the photoactive nature of the CdSe quantum dot film, which presents a couple of distinctive device design challenges in that it is undoped, insulating, and nonuniform. Most likely the CdSe film does not provide complete coverage of the substrate surface. Our objective is to take this film and make a device that will suppress unwanted current flow in the dark, yet be able to efficiently coax excited electrons and holes out of the device when under illumination. This type of rectification is accomplished quite well by a reverse biased p-n junction,

which is ubiquitous in the field of photodetectors. However, the quantum dot film, in its undoped form, cannot form a p-n junction directly and so rectification must be imposed externally. Without some form of rectification, a low shunt resistance would arise, either from direct contact between the metal electrodes or direct injection of carriers into the quantum dots. Low shunt resistance adds a much larger drift current noise term to the intrinsic thermal generation current noise  $I_n$  and thereby reduces detection sensitivity.

### 2.5.1 The concept of blocking layers

In Figure 2-7, we illustrate the basic concepts of device operation of our tri-layered p-i-n-like structure. The contact layers serve the dual purpose of transporting charge out of the device and blocking charge from entering the device. When the Fermi level of a semiconductor is aligned with the work function of a metal electrode, charge of only one polarity can enter and exit freely at that electrode. Charge of the opposite polarity is blocked by a large energy barrier at the interface. If we combine this rectifying contact with one at the other contact, we create a rectified device because charge is blocked at both electrodes in reverse bias, but allowed to enter in forward bias. An assumption made in Figure 2-7 is that the blocking layers are sufficiently conductive that there is little voltage drop across these regions, leaving most of the applied voltage to act on the middle, insulating layer. Another assumption is that there are no defect states in the blocking layers that could transport charge and thus limit its blocking capability [51]. We will be able to test these assumptions by analyzing the current-voltage characteristics.

By choosing p-type and n-type contact layers that are appropriate for CdSe, we form something akin to the p-i-n diode structure in Figure 2-7 and therefore limit conduction in reverse bias. Non uniformities in the CdSe film will no longer cause shunting as long as the p-type and n-type layers provide complete coverage. Employing wide band gap contact layers like  $\text{TiO}_2$  and TPD enables direct measurement of the CdSe absorption and photoresponse.

Energy level alignment of the ITO/ $\text{TiO}_2$ /CdSe/TPD/Ag or Au photodetector is



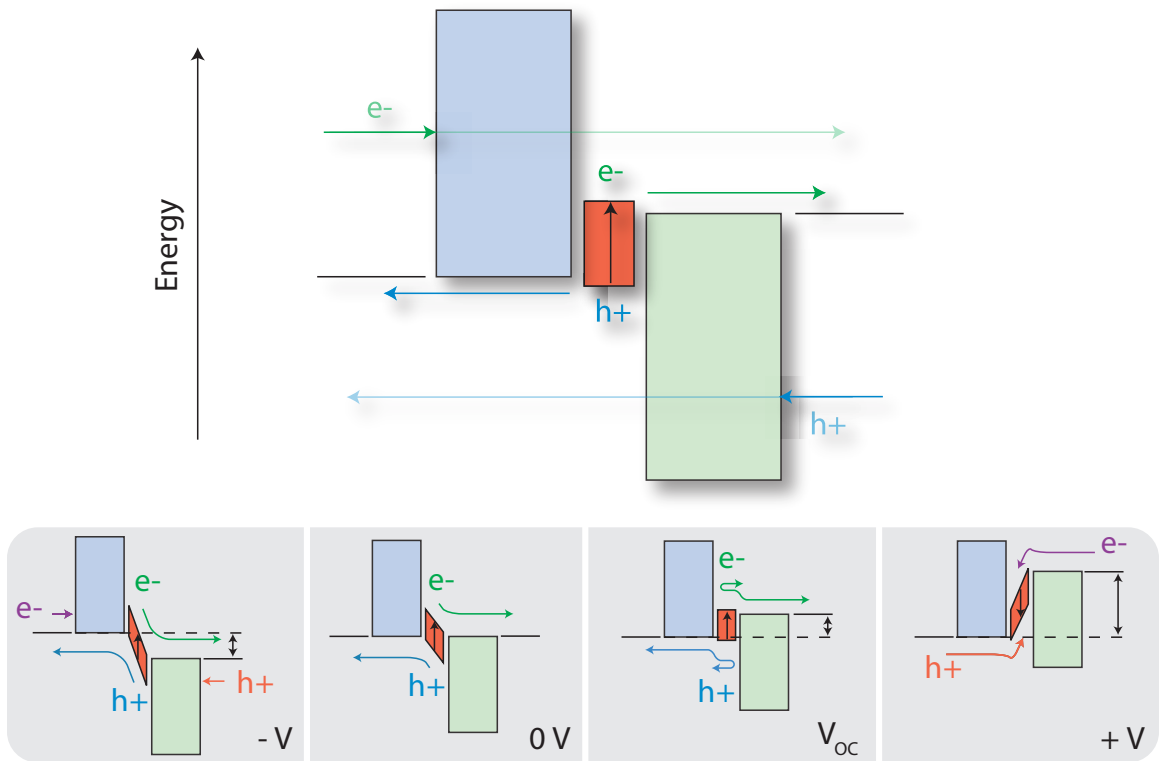


Figure 2-7: Idealized pin heterojunction energy band diagram with bias dependence. Under reverse bias, photogenerated charge is swept away to the contacts, while injected charge is blocked from entering the device.

depicted in Figure 2-8. In reverse bias, hole injection from the ITO electrode into  $\text{TiO}_2$  is suppressed because of the large potential step at the interface. Likewise, electron injection from the gold electrode into TPD is limited due to the potential barrier at that interface. Therefore, dark current in reverse bias should be largely due to generated carriers in CdSe. Note that electron transfer from CdSe to  $\text{TiO}_2$  is not energetically favorable, at least when neglecting interface effects. In future devices, it may be possible to select materials such that there is a downward step in energy upon transfer to the n-type transport layer.

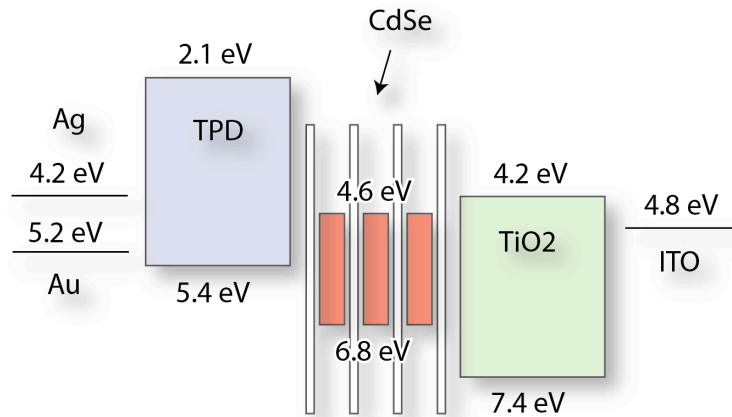


Figure 2-8: Energy level alignment in our device.

## 2.6 Summary

This chapter introduced our quantum dot photodetector device architecture and material system. We also developed two key concepts for photodetectors. First, the ideal p-n junction was described and the notions of rectification, series resistance and shunt resistance were discussed. Second, the concept of charge injection and charge blocking at electrodes was introduced and the implications for device behavior were highlighted. These concepts will reappear later in the thesis as we discuss the empirical data.

# Chapter 3

## Device fabrication

In the last chapter, we introduced the materials used in our quantum dot photodetector design and touched upon the basic operational principals of the tri-layered heterostructure device. In this chapter, we describe the processes used to fabricate the device in the lab.

### 3.1 The $\text{TiO}_2$ layer

Two of the most widely used deposition techniques for metal oxide thin films are *sol gel deposition* and *radio frequency (rf) sputtering*. Sol gel processing is a common way of depositing thin inorganic or inorganic/organic protective coatings. It is a low temperature synthesis process based on the hydrolysis and condensation reaction of organometallic compounds in alcoholic solutions. The resulting gel is a dispersion of nanometer or micron sized cross-linked particles, and is suitable for spin casting. For device applications, sol gel films are desirable because of their ability to be patterned on the nanometer scale with low-cost methods such as PDMS stamping [39]. Metal oxide films can also be obtained by rf magnetron sputtering, which is a more reproducible deposition method and affords greater control over thickness and doping concentrations.

### 3.1.1 Solgel deposition of TiO<sub>2</sub> films

The sol gel deposition process shown in Figure 3-1 is as follows. By volume, 4 parts of the TiO<sub>2</sub> precursor Titanium ethoxide, C<sub>8</sub>H<sub>20</sub>O<sub>4</sub>Ti (Gelest), is added to a stirring solution of 40 parts ethyl alcohol, which contains 1 part water and three drops of hydrochloric acid. The TiO<sub>2</sub> precursor reacts with water to form the reactive monomer (RO)<sub>3</sub>TiOH that in turn reacts with other monomers to form a sol. Heating the solution for 45 minutes at 60°C aids the gelation (cross-linking) process, during which the viscosity gradually increases. The TiO<sub>2</sub> precursor is spin coated at 2000 rpm onto a patterned ITO glass substrate that is masked with scotch tape. After deposition, the tape is removed and the sample is heated at 100°C for 30 minutes to allow further cross-linking and dehydration of the TiO<sub>2</sub> matrix. Annealing under vacuum at 450°C for 30 minutes allows the growth of crystalline regions of the anatase phase (densification). The resulting films are transparent, smooth and approximately 100 nm thick, with surface features smaller than 8 nm.

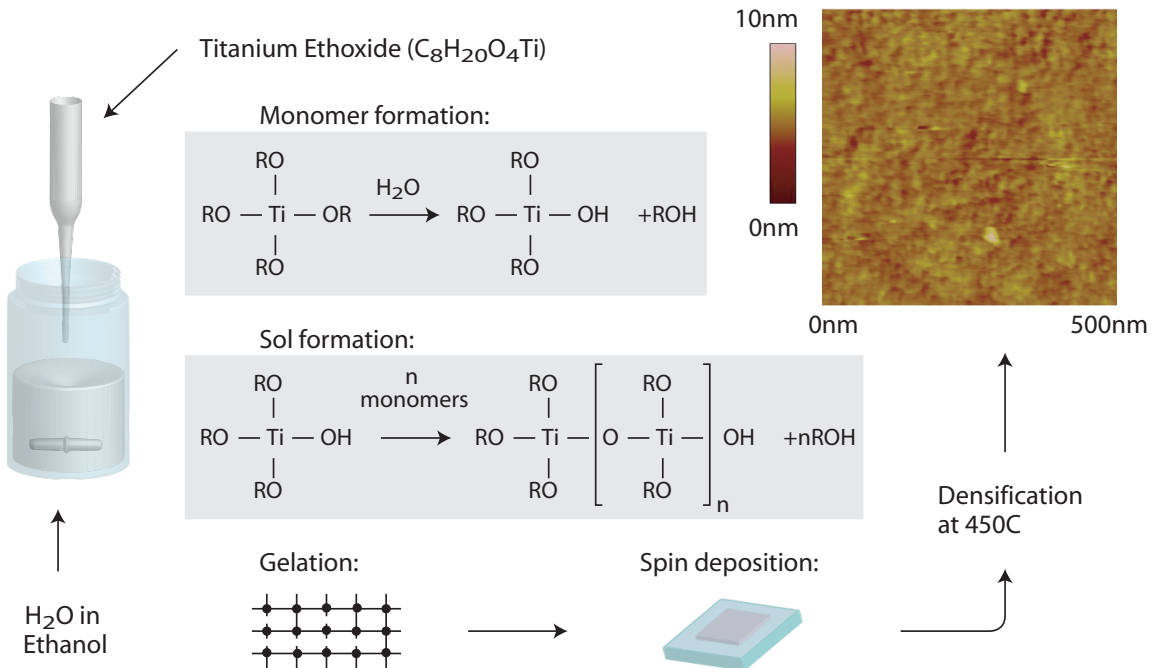


Figure 3-1: TiO<sub>2</sub> thin film deposition process via sol-gel and AFM image of the surface of the resulting film.

### 3.1.2 Radio frequency sputter deposition of $\text{TiO}_2$ films

A magnetron sputter deposition chamber contains two electrodes, two magnets, a turbo pump with a variable aperture gate valve and gas flow valve (Figure 3-2).

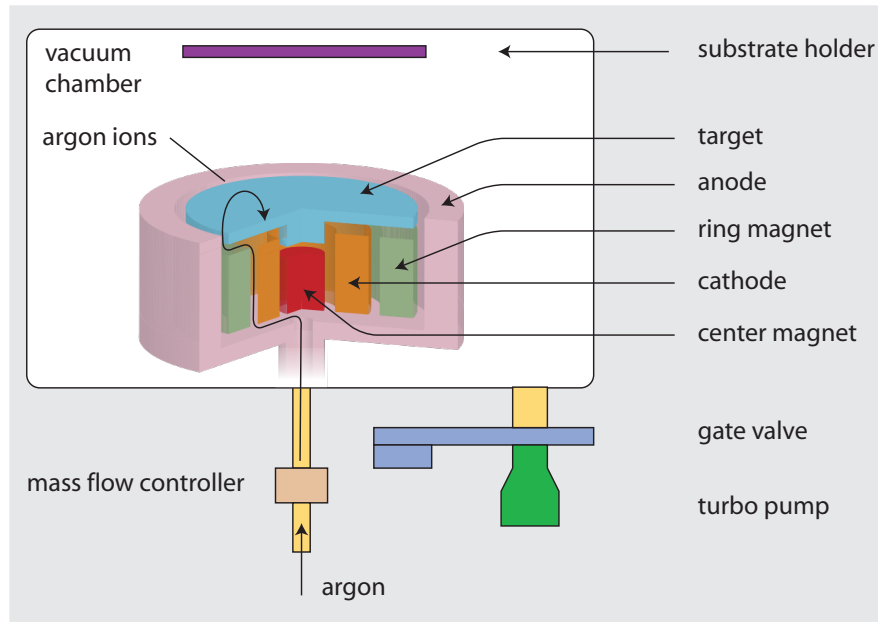


Figure 3-2: Schematic diagram of RF-powered sputter deposition system.

The material to be deposited (the target) is placed on top of the cathode. The chamber is filled with an inert gas like Argon (Ar) and several thousand volts is applied across the electrodes, creating a plasma of equal numbers of positive Ar ions and free electrons. When the plasma is struck, emission from the relaxation of excited Ar ions can be seen through the chamber viewport. The positive Ar ions are accelerated toward the target and, upon collision with the surface, dislodge atoms from the target. The free atoms then travel throughout the chamber and deposit themselves on the substrate. The magnets are designed to confine the plasma to the area above the target, sparing the substrate from ion and electron bombardment. In rf sputtering, an AC field is applied instead of a DC field. The AC field is useful for sputtering insulating target materials that will build up charge over a time scale of a couple of microseconds. An AC voltage in the MHz range is faster than this build

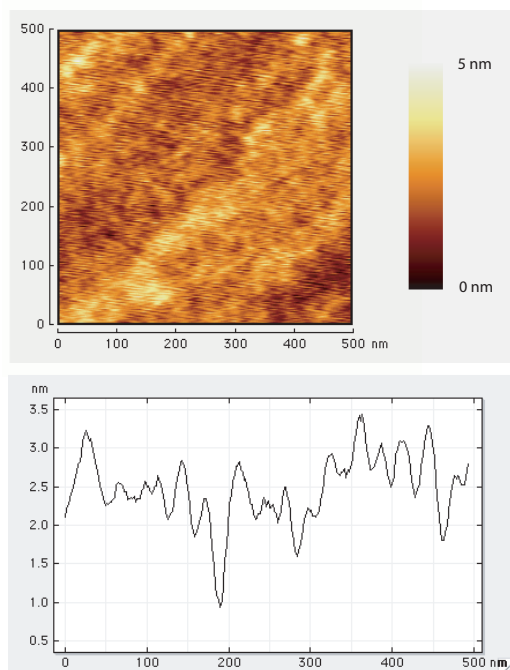


Figure 3-3: AFM image of a sputtered  $\text{TiO}_2$  film.

up, allowing for negative free electrons to neutralize the surface and thereby maintain current flow. The amount of gas in the chamber is controlled by the rate of gas flow into the chamber and the aperture of the gate valve. The gas pressure must be high enough to sustain the plasma, yet low enough that scattering does not prohibit free atoms from reaching the substrate. The resulting films are dense and smooth, with feature sizes on the order of a couple of nanometers (Figure 3-3).

## 3.2 The CdSe layer

The CdSe quantum dots used in this work are prepared by David Oertel from the Bawendi group, who pioneered in the field of colloidal quantum dot chemistry. For a detailed description of the quantum dot synthesis, see [23]. Films of CdSe quantum dots are deposited from hexane onto  $\text{TiO}_2$  coated ITO-glass substrates by spin coating under a nitrogen atmosphere. Post-deposition chemical treatment of the CdSe film is accomplished by immersing the film in butylamine for 10 minutes prior to heating

at 80°C for one hour in order to drive off the solvent.

### **3.3 Purification of organic small molecules**

Some organic materials contain impurities as received from the supplier. These impurities can be removed by thermal gradient sublimation. Appendix D describes the procedure developed by Debbie Mascaro for purifying organic small molecule powders. Following this procedure results in high-purity organic material suitable for device manufacture. We use a turbo pump to maintain high vacuum inside a quartz purification tube (Figure 3-4). The tube is heated by a tube oven capable of applying a temperature gradient across the tube.

High-purity material is obtained in the following way. The organic source material is heated above its sublimation temperature in Zone 1 and is deposited in Zone 2 where the temperature is kept below the sublimation temperature. Residual impurities remain in Zone 1 and volatile impurities collect in Zone 3, which is kept at a temperature well below that of Zone 2. The high-purity organic can be collected off the sidewalls of the quartz insert tube with a clean spatula.

### **3.4 The complete device growth process**

We begin with a half-inch substrate of ITO coated glass. For the case of sol gel layers, the TiO<sub>2</sub> is deposited, sintered and then transferred to a nitrogen glove box for CdSe spin casting. In the case of sputtered TiO<sub>2</sub>, substrates are transferred from the sputterer to the glove box via a vacuum line and a load lock. After CdSe deposition and treatment in the glove box, the substrates are reloaded into the vacuum line and transferred to the evaporator, where TPD and the top electrode are put down. We use either gold or silver top contacts. The complete device is shown in Figure 3-5.

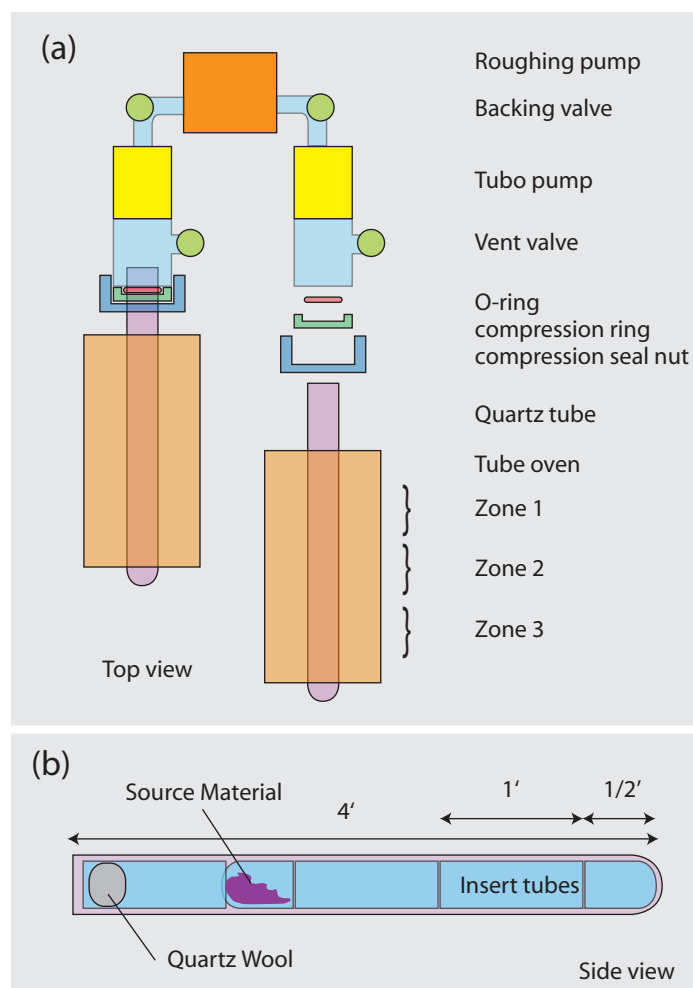


Figure 3-4: Diagram of thermal gradient sublimation system used to purify small molecule organic powders.



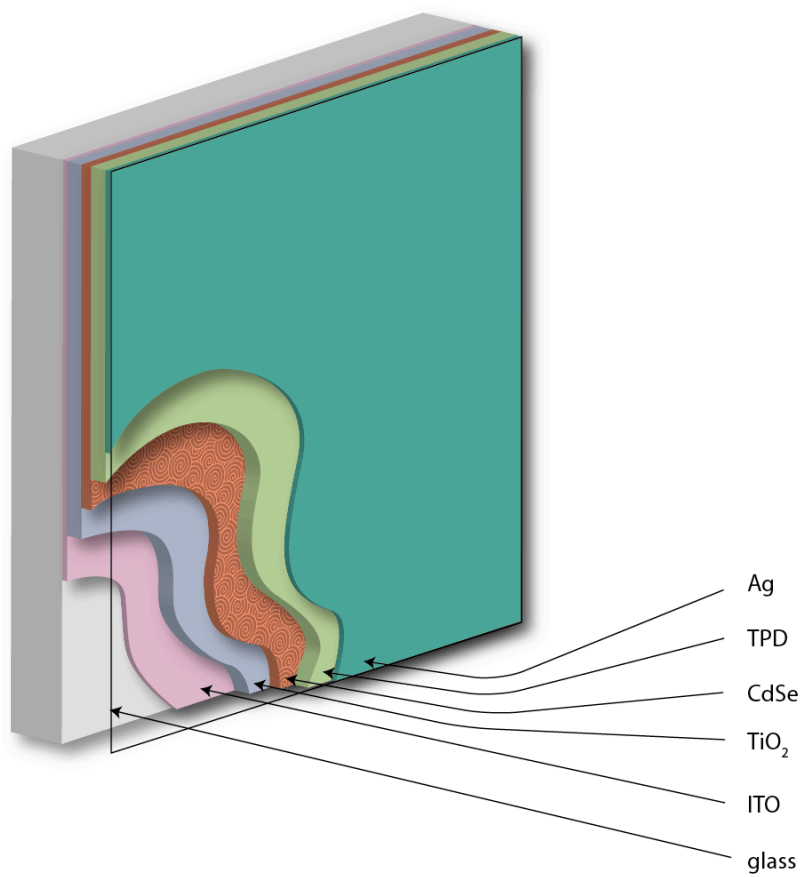


Figure 3-5: Diagram of colloidal CdSe quantum dot photodetector device.

### 3.5 Probe fixture and patterning

In order to test the device in nitrogen or at low temperature, we have designed a probe fixture and a masking system with displaced contact pads for each device. The probe fixture (Figure 3-6) is designed to house the substrate and make contact to the device via spring-loaded gold pins (not shown). The gold pins make contact with the underlying ITO pads, which in turn are connected to the device top electrode. There are four devices per half-inch substrate, each of area 0.1 inch x 0.1 inch = 0.064516 cm<sup>2</sup>. The active device area is located at the intersection between the bottom ITO layer and the top electrode, as shown in Figure 3-7. The ITO is patterned as described in Appendix A. The tolerance of the masking setup is well within the limits of the substrate holder/mask holder system, ensuring that the active device area is exactly the same from run to run.

### 3.6 Summary

Device growth for this work is accomplished using a number of different techniques, including sol-gel processing, thermal evaporation, rf sputtering and spin casting. The whole device is manufactured either under vacuum or nitrogen, without being exposed to oxygen.

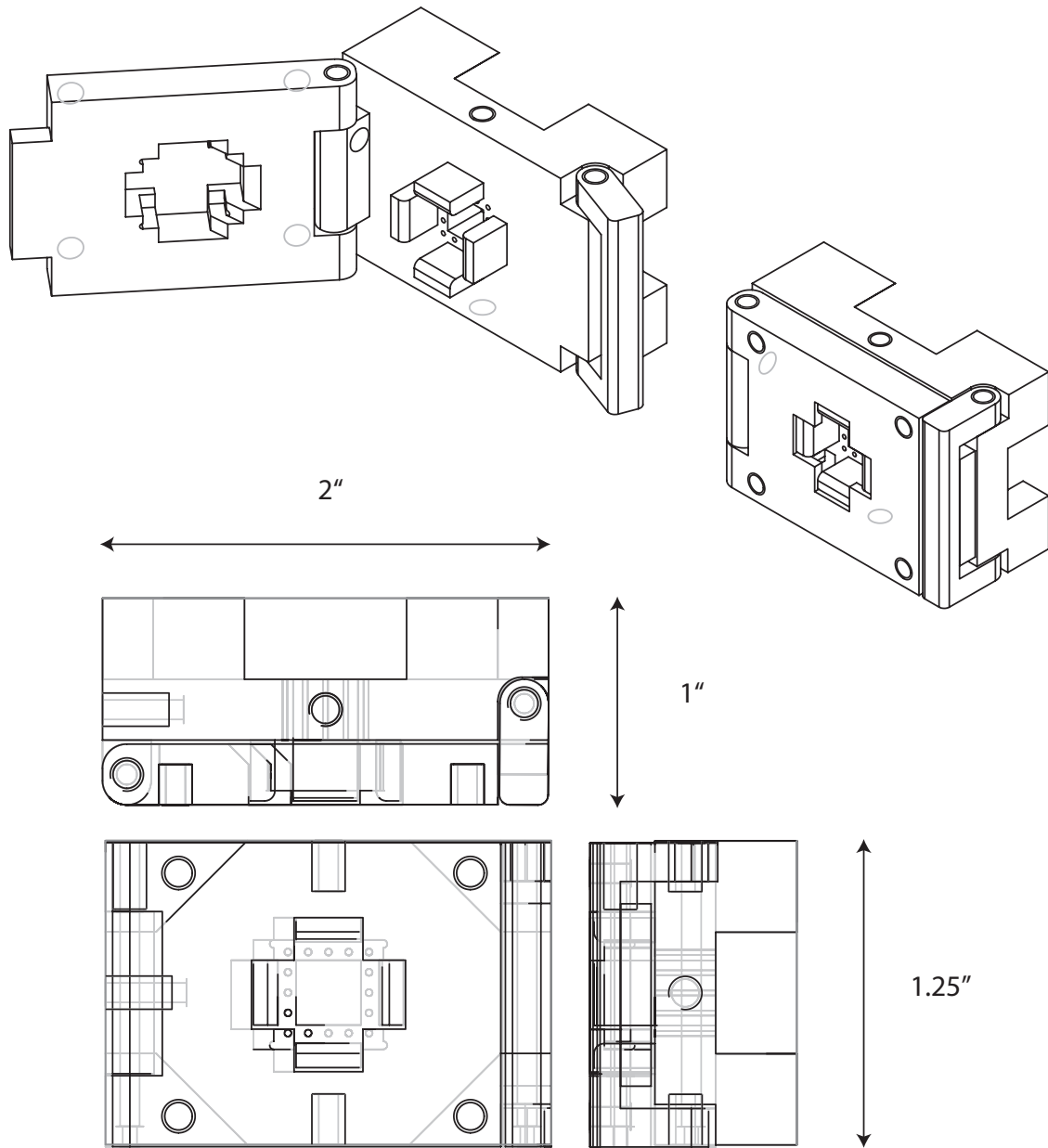


Figure 3-6: Drawings of the probe fixture used to test photodetectors on half-inch substrates.

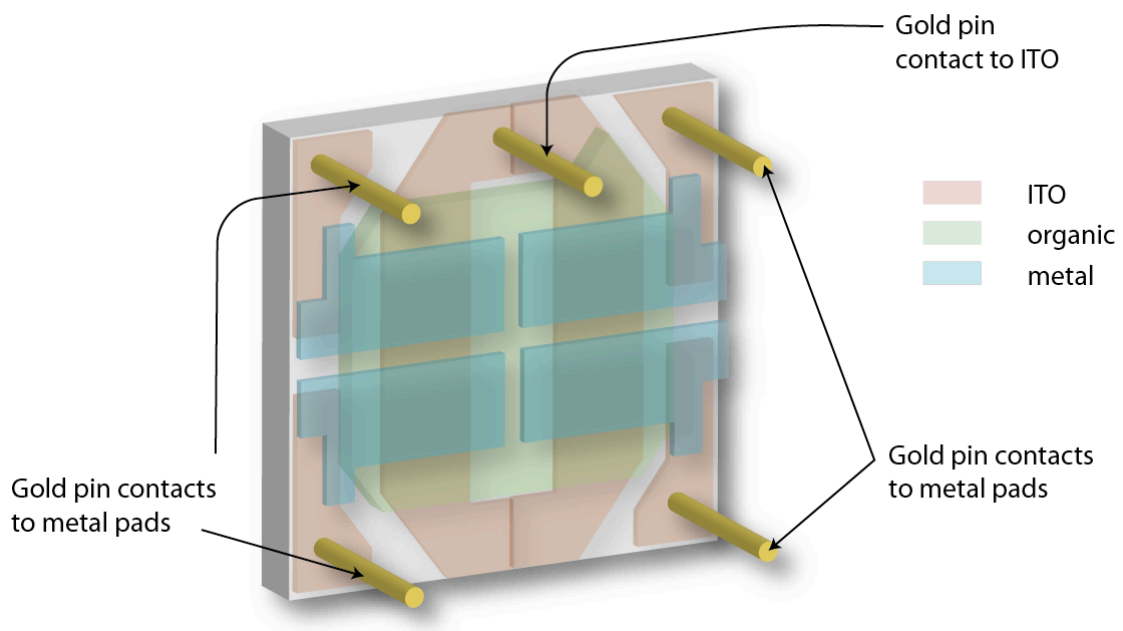


Figure 3-7: Electrodes and active layers of the device are patterned in order to make contact with gold pins from our probe fixture.

# Chapter 4

## Current-voltage characteristics under illumination

In the previous chapter, we described the fabrication techniques used to build a quantum-dot-based diode structure. This chapter will focus on the first of three electrical characterization methods: current-voltage (i-v) measurements. We begin with a description of the experimental apparatus and then present data showing a substantial photocurrent.

### 4.1 Measurement apparatus

We have developed two systems for measuring i-v curves, one in which devices are measured in ambient atmosphere, and one in which devices are tested in a nitrogen-atmosphere glove box. Both measurements described below use a white light source. However, the Xenon source, which provides illumination for the ambient setup, emits UV radiation while the Halogen source, used in the nitrogen setup, does not.

#### 4.1.1 Measurement in atmosphere

When device characterization is performed in ambient atmosphere, care must be taken to measure quickly before degradation becomes apparent. Photo-oxidization of

organic components, oxidation of metal contacts and delamination in humid environments can all limit device lifetimes. An additional worry, especially when measuring photo-responsive devices, is that the presence of oxygen trap sites will degrade performance. These traps can hinder photocurrent either by serving as recombination centers or by generating internal electric fields, counter to those required for proper device operation.

Incident light is generated by a 40 Watt Xenon bulb powered by a programmable HP DC power supply, which is used as a 2x voltage amplifier for the output from voltage source 1 (VS1) of an HP Semiconductor Parameter Analyzer 4145B (Figure 4-1). Current-voltage characteristics of the illuminated device are measured by source-measurement unit (SMU) channels 2 and 3 of the HP. Channel 1 is not used because it is nonfunctional.

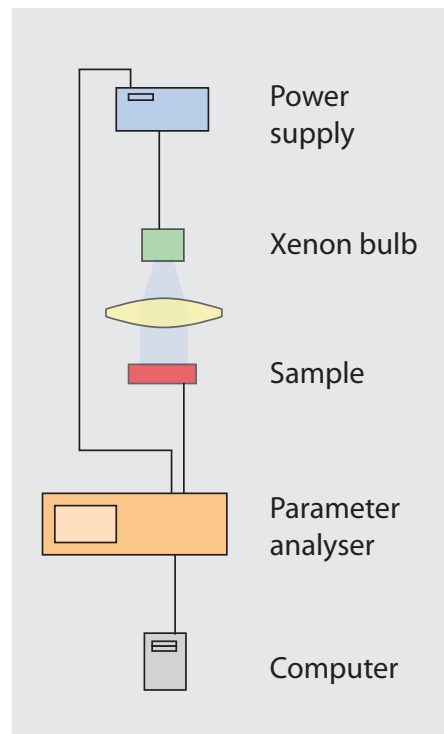


Figure 4-1: Diagram of setup for current-voltage measurements taken in ambient atmosphere.

To roughly characterize the light intensity incident on a sample, we use a Newport

818-UV photodiode with an OD 3 filter. The responsivity of the photodiode with filter attached is  $3.5 \times 10^{-4}$  A/W across almost all of the lamp emission spectrum. The surface area of the detector is  $1 \text{ cm}^2$ .

### 4.1.2 Measurement in nitrogen

After noticing that our CdSe devices were degrading quickly during measurements, we built a measurement setup located inside an inert nitrogen-filled glove box. This setup, depicted in Figure 4-2 allows us to test devices without any apparent degradation. In the glove box, substrates are placed in a probe fixture (described in section 3.5) and connected via electrical feedthroughs to the output of a Keithley 2400 source-meter, which is used to apply bias and read current. Illumination is provided by a halogen lamp located outside the glove box. The intensity of incident light was not measured.

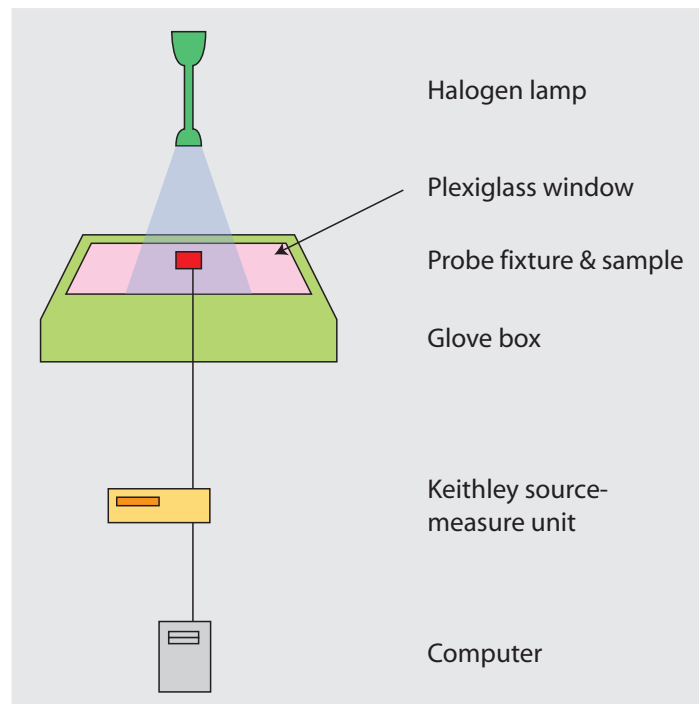


Figure 4-2: Diagram of setup for current-voltage measurements taken in a nitrogen-filled glove box.

### 4.1.3 Sign convention

It is worth mentioning that the sign convention we've adopted results in the opposite electrical connection of that used for organic LEDs. As we've seen in section 2, the p-side of a p-n diode is grounded while the n-side is positive, resulting in positive current flowing under positive bias and almost no current (the saturation current  $I_{sat}$ ) flowing under reverse bias. In order to keep this convention, we ground the ITO electrode and connect the positive lead of the source-measure-unit (SMU) to the top metal electrode (Figure 4-3).

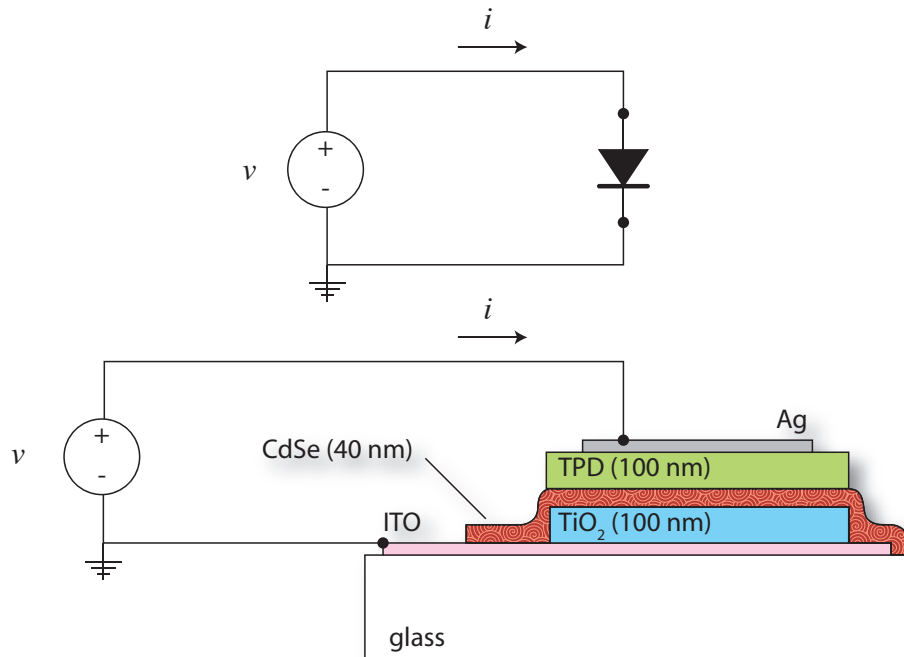


Figure 4-3: To preserve the same polarity as a pn junction diode, we connect the positive lead of a voltage supply to the top metal electrode and the ground lead to ITO. Note that this configuration is the opposite of that used to apply voltage to an organic LED.



## 4.2 Experimental results

In this section, we will see how electrical characteristics change in a predictable way when a quantum dot multilayer and a titanium dioxide anode is present. From these i-v curves, we can ascertain (a) to what extent charge injection from the electrodes is blocked in reverse bias; (b) if charge injection is possible in forward bias; and (c) if transport is affected by the presence of a quantum dot layer. Additionally, we will show how illumination influences the i-v characteristics.

The devices presented in this chapter are given in Table 4.1.

Table 4.1: Device structures presented in this chapter.

Device structure	Environment	Comments
ITO/TiO <sub>2</sub> (100nm)/TPD(250nm)/Au	Air	solution deposition
ITO/TiO <sub>2</sub> (100nm)/TPD(100nm)/Ag	Air	
ITO/TiO <sub>2</sub> (100nm)/CdSe(80nm)/TPD(100nm)/Ag	Nitrogen	
ITO/TiO <sub>2</sub> (100nm)/CdSe(40nm)/TPD(100nm)/Ag	Nitrogen	butylamine treatment
ITO/CdSe(80nm)/TPD(100nm)/Ag	Air	

### 4.2.1 Characteristics of control devices without a quantum dot film

We begin with the i-v characteristics of the ITO/TiO<sub>2</sub>(100nm)/TPD(250nm)/Au device, shown in Figure 4-4. The TiO<sub>2</sub> is spin cast via the sol gel method described in section 3.1.1. The TPD was dissolved in chloroform and spin cast at 2000 rpm. In reverse bias, the dark current is low, as anticipated, but begins to rise strongly above -0.2 V. Under white light illumination, the photocurrent saturates at around +0.5 V and remains nearly bias independent at negative voltages, a trademark of interfacial exciton dissociation and low parasitic shunt conductance. The open circuit voltage is around 0.6 V, which is low compared to similar devices structures in the literature [52, 35]. In forward bias, the dark current follows a  $V^3$  dependence, which is indicative of space charge limited current with shallow traps. Under illumination, the

forward bias current departs from the ideal diode model in that the current becomes intensity dependent. Essentially, the series resistance is lowered with increasing intensity. There are two possible explanations. First, excited carriers generated in the TPD or  $\text{TiO}_2$  films or both may be filling traps and thereby changing the distribution of trapped charge throughout the device, which could lead to increased current flow. Second, the accumulation of excited charge at the  $\text{TiO}_2$ /TPD interface may be increasing the rate of recombination across the interface, which may be the current limiting process.

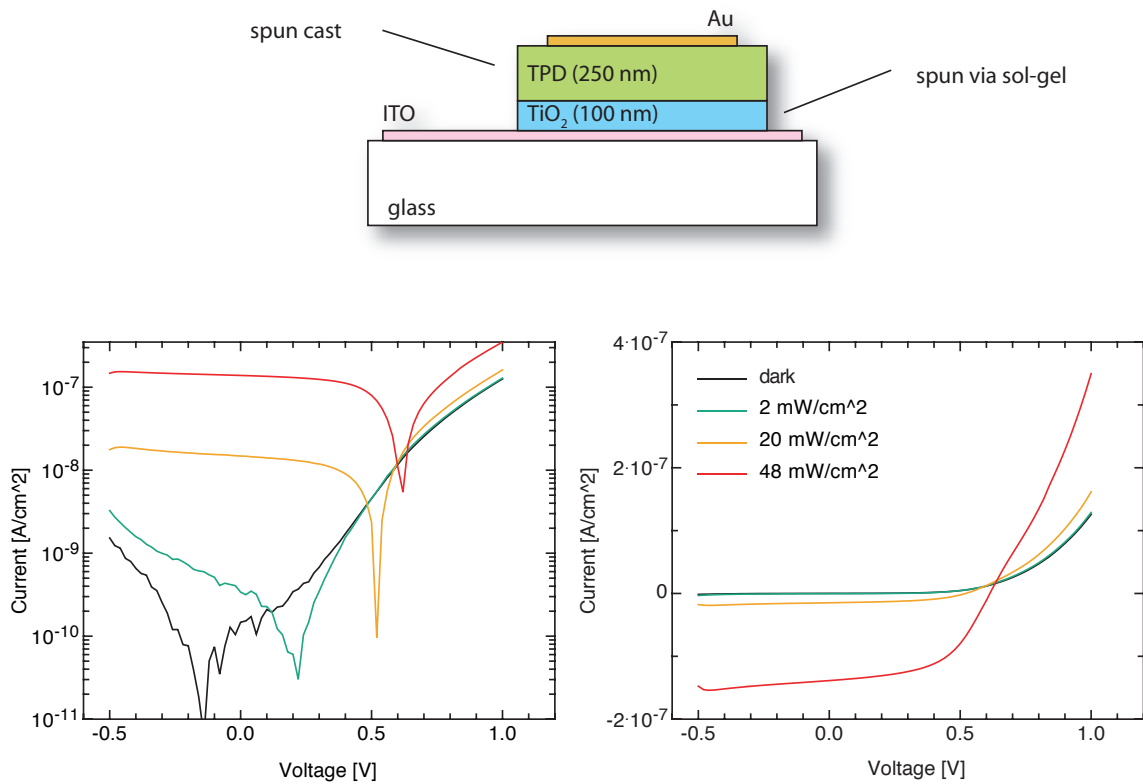


Figure 4-4: Log-linear i-v characteristics and linear i-v characteristics of a device consisting of a  $\text{TiO}_2$  layer spun via sol-gel and a spun TPD layer. Good rectification and current saturation under illumination indicate that the  $\text{TiO}_2$  and TPD layers form charge blocking contacts.

The  $\text{ITO}/\text{TiO}_2(100\text{nm})/\text{TPD}(100\text{nm})/\text{Ag}$  device, shown in Figure 4-5, displays similar characteristics as the previous device, but the fragility of the device prevented us from taking data at higher voltages. In this device, the  $\text{TiO}_2$  was rf sputtered

and the TPD was deposited by thermal evaporation. The essential features of the i-v characteristics are similar to those of the solution cast device. The dark current is at the instrument noise level in reverse bias and the current in light saturates readily. One aspect is exceptional, however. The open circuit voltage approaches 0.4 V, although one would expect no open circuit voltage if considering only the work function difference between  $\text{TiO}_2$  (4.2 eV) and Ag (4.2 eV). This value for open circuit voltage is evidence for the presence of a dipole at the interface between  $\text{TiO}_2$  and TPD resulting from accumulation of dissociated carriers, as proposed by Ramsdale [53] and Gregg [54].

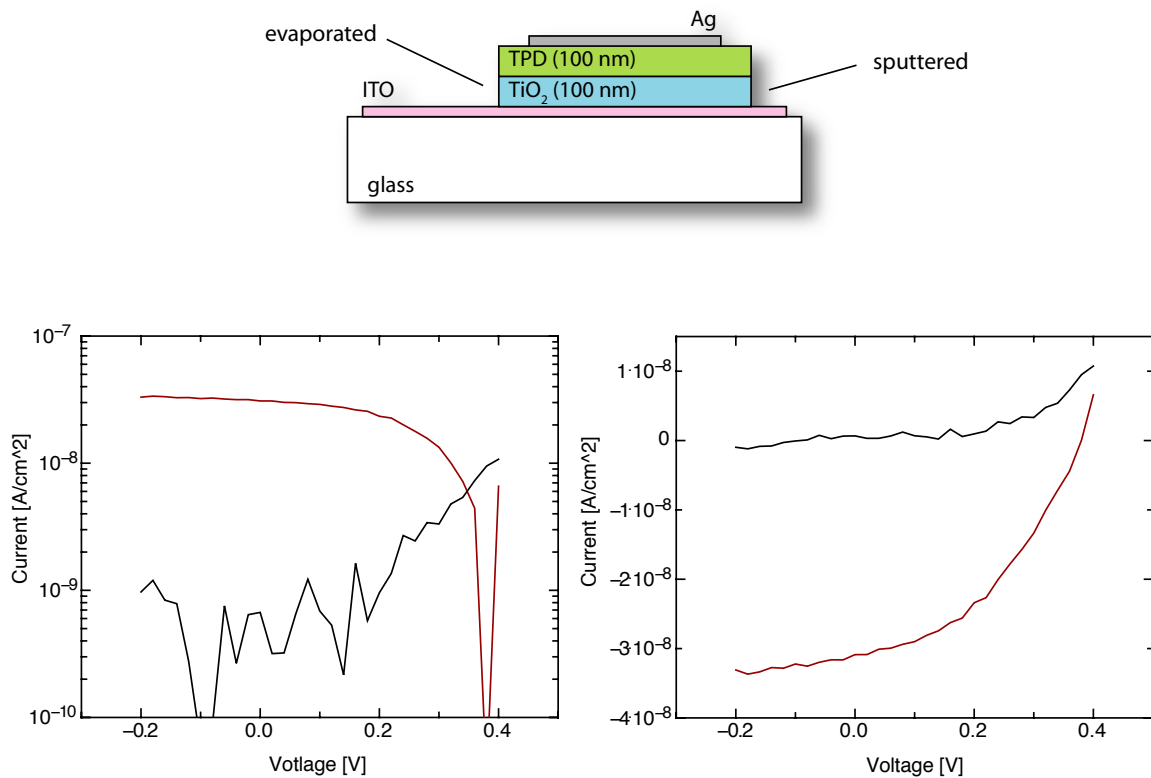


Figure 4-5: Log-linear i-v characteristics and linear i-v characteristics of a device consisting of a sputtered  $\text{TiO}_2$  layer and an evaporated TPD layer. At low voltages shown here, the device displays low dark current (black line) and current saturation under illumination (red line).

Figure 4-6 illustrates the inability of the 100 nm TPD devices to withstand moderate applied voltage. After an i-v scan down to -0.5 V, the dark current jumps from

below the instrument noise level to values that are higher than the initial photoresponse in Figure 4-5. One possible interpretation is that the TPD film is damaged during the evaporation of the Ag contact. Durr [55] has observed that metal filaments from an evaporated metal top contact can penetrate into organic films. At high bias, some of these filaments will punch through the organic film, causing a lowering of the shunt resistance and an increase in leakage current.

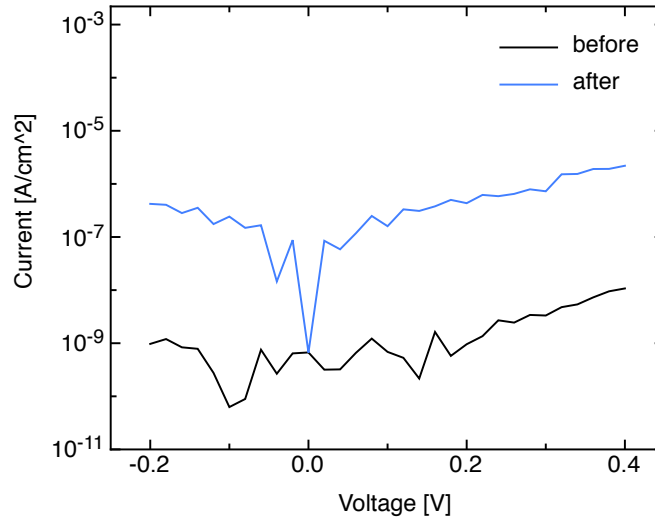


Figure 4-6: Log-linear i-v characteristics and linear i-v characteristics of the same  $\text{TiO}_2/\text{TPD}$  device before and after application of 0.5 V of reverse bias. The change represents a tendency to break down at low bias voltages.

#### 4.2.2 Devices containing a CdSe quantum dot film

The i-v characteristics of an  $\text{ITO}/\text{TiO}_2(100\text{nm})/\text{CdSe}(80\text{nm})/\text{TPD}(100\text{nm})/\text{Ag}$  device are shown in Figure 4-7 and the i-v characteristics of an  $\text{ITO}/\text{TiO}_2(100\text{nm})/\text{CdSe}(40\text{nm})/\text{TPD}(100\text{nm})/\text{Ag}$  device, where the CdSe layer has been treated with butylamine, are shown in Figure 4-8. Both sets of measurements were taken under nitrogen and illuminated through a Plexiglas window that strongly filters the UV components of the halogen light source. Since  $\text{TiO}_2$  and TPD absorb only in the UV, we expect the CdSe to be the only photo-active layer.

In the untreated device, we observe a slight sensitivity to light. However, a cou-

ple of instrumentation issues complicate the interpretation of the i-v characteristics. First, a large dc offset ( $\sim 5 \times 10^{-10}$  A corresponding to  $\sim 7 \times 10^{-9}$  A/cm<sup>2</sup>) is present in the Keithley 2400 source-meter. Second, the impedance of the device in the dark is larger than the internal impedance of the source-meter, which is around 2 G $\Omega$ . Thus, the true dark current is less than the measured dark current. The large hysteresis and absence of open circuit voltage are most likely attributable to the instrumentation deficiencies just mentioned.

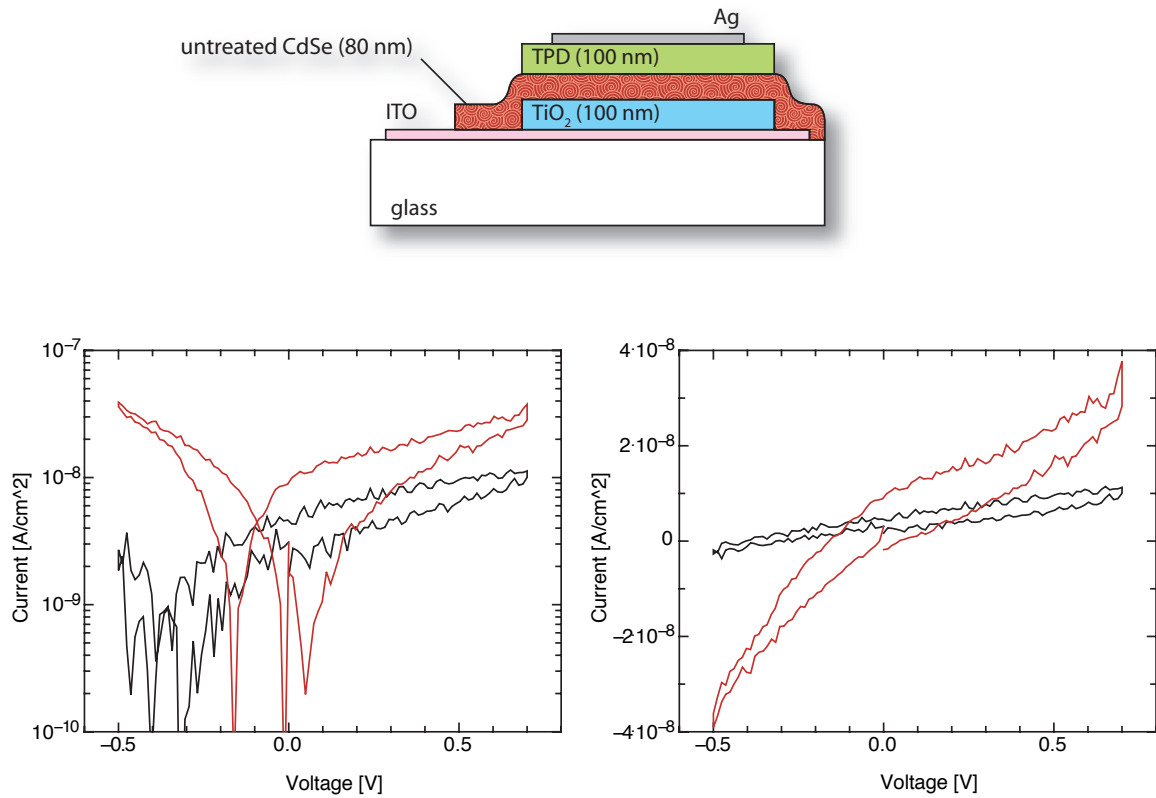


Figure 4-7: Log-linear i-v characteristics and linear i-v characteristics of a CdSe device measured under nitrogen. A modest current under illumination (red line) from a halogen light source is visible, but does not saturate before breakdown. Hysteresis is most likely due to instrument drift.

The treated device also displays a dark current dominated by the internal resistance of the Keithley, but the current under illumination is more than an order of magnitude greater than that of the untreated device. The open circuit voltage is around 0.4 V, in agreement with the control device. Under forward bias, there is no

effect of light on current. In the linear i-v plot, the photocurrent crosses the x-axis at a shallow angle, indicating a large series resistance. Since the control device without the CdSe layer has a low series resistance, we can attribute this large series resistance to the CdSe layer.

In order to improve device efficiencies, series resistance in the CdSe will have to be dealt with. We will see in chapter 5 that at 40 nm, the treated CdSe absorbs only 10% of the incident light. To absorb a larger percentage of light, a thicker CdSe layer is needed and will thereby impose an even larger series resistance constraint.

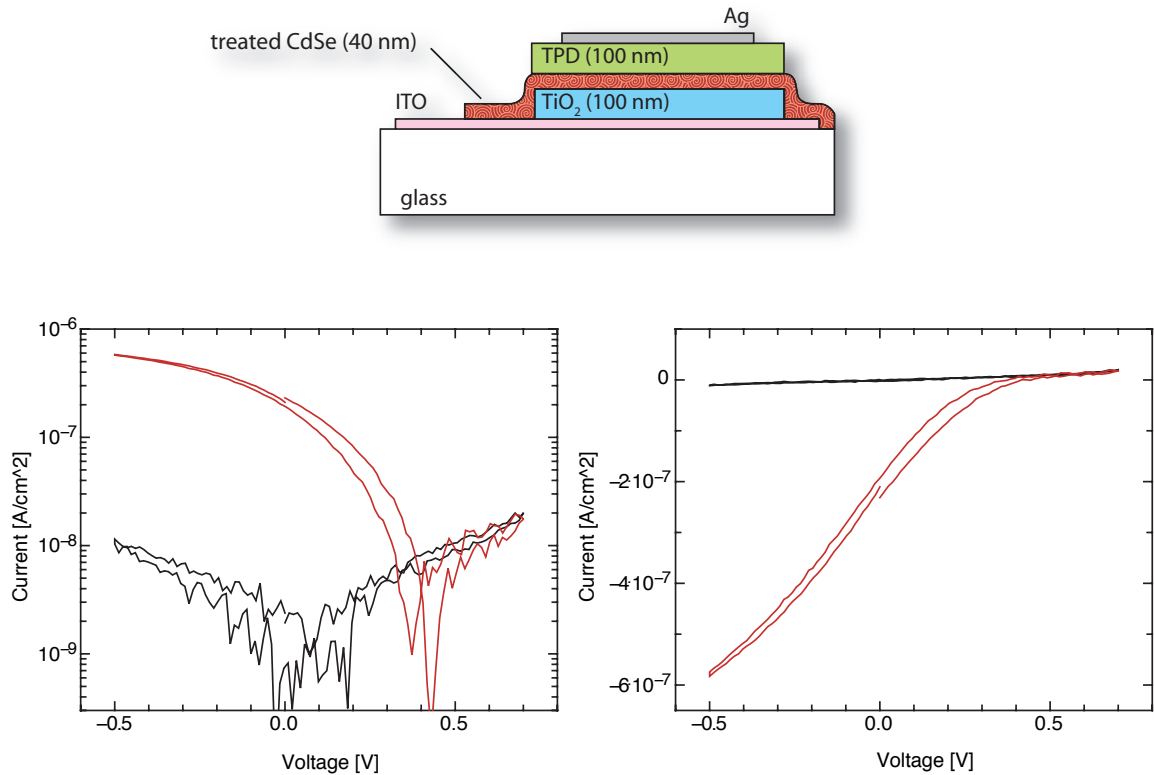


Figure 4-8: Log-linear i-v characteristics and linear i-v characteristics of a treated CdSe device measured under nitrogen. Significant current is apparent under illumination from a halogen source (red line), but is limited by high series resistance.

Figure 4-9 displays the device structure and i-v curve for the same device containing an untreated CdSe film, but missing the TiO<sub>2</sub> layer. As expected, the blocking characteristics are absent and the i-v characteristics are linear. Holes inject from

the Ag electrode to the TPD and subsequently either inject into the CdSe or bypass the CdSe entirely via pinholes in the CdSe film. At these low current densities, Ohmic conduction through the TPD is not surprising, but at higher current density we should observe space charge limited current if indeed the TPD is transporting charge. Unfortunately, we were unable to reliably probe at higher voltages due to irreversible breakdown. No light sensitivity is observed because the photocurrent is drowned out by the dark current.

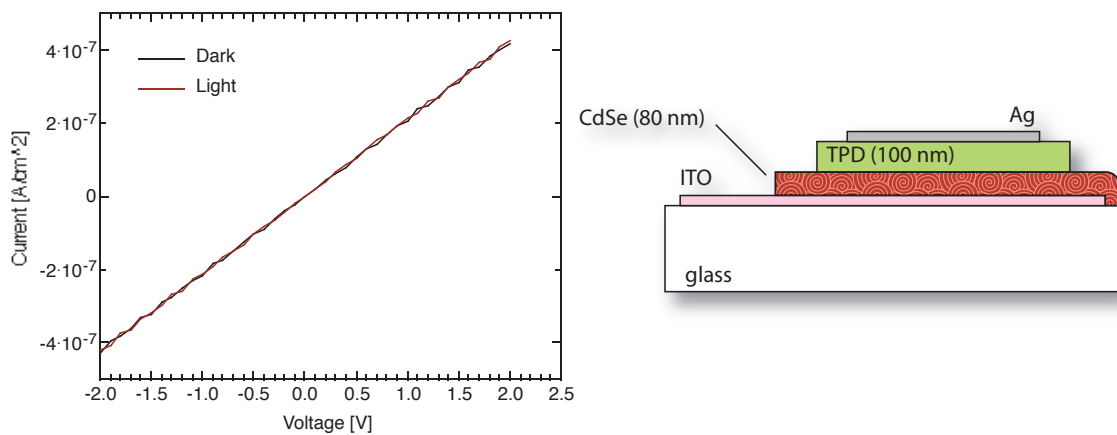


Figure 4-9: Current-voltage characteristics of a CdSe/TPD bi-layer device displays neither rectification nor sensitivity to light.

### 4.3 Summary

We have presented the i-v characteristics of the quantum dot photodetector and control devices without a quantum dot layer. From the control device curves, we obtain good diode characteristics, high shunt resistance and low series resistance. The addition of a quantum dot layer increases the resistance of the device substantially. Chemical treatment of the CdSe layer improves the response to light by at least an order of magnitude.





# Chapter 5

## Photocurrent spectra

In the previous chapter, we looked into the current-voltage characteristics of quantum-dot-based diode structures and found a sizable voltage and current response under illumination. This chapter will focus on the spectral dependence of the photocurrent signal, using the second of three electrical characterization methods: photocurrent spectra. We begin with a description of the experimental apparatus and then present data showing that the photocurrent spectrum tracks the absorption signature of the CdSe quantum dots.

### 5.1 Measurement apparatus

Photocurrent spectra provide two important pieces of information about the operation of a photodetector: wavelength dependence and quantum efficiency. We have built a custom LabView-based program that interfaces with a monochromator and a lock-in amplifier, and coordinates the measurement of photocurrent at wavelengths in the 300 nm to 800 nm range of the electromagnetic spectrum. Quantum efficiency (described below in more detail) is obtained by comparing the signal to that of a calibrated reference photodetector.

### 5.1.1 Description of measurement

A narrow wavelength band of light is generated by a white Oriel Instruments Xenon arc lamp light source and an Oriel Instruments Cornerstone 1/8 m 74000 monochromator. The monochromatic light beam is chopped by a Stanford Research Systems SR540 Chopper and is focused down to a small point at the sample surface (Figure 5-1). The chopping frequency is output by the chopper to the Stanford Research System SR830 DSP lock-in amplifier's reference channel. The lock-in's circuitry acts as a narrow band filter, measuring only the current from the input signal that is oscillating at the reference frequency. Thus, the lock-in amplifier provides a convenient way to measure photocurrent while excluding electrical noise and stray signal due to the room lights.

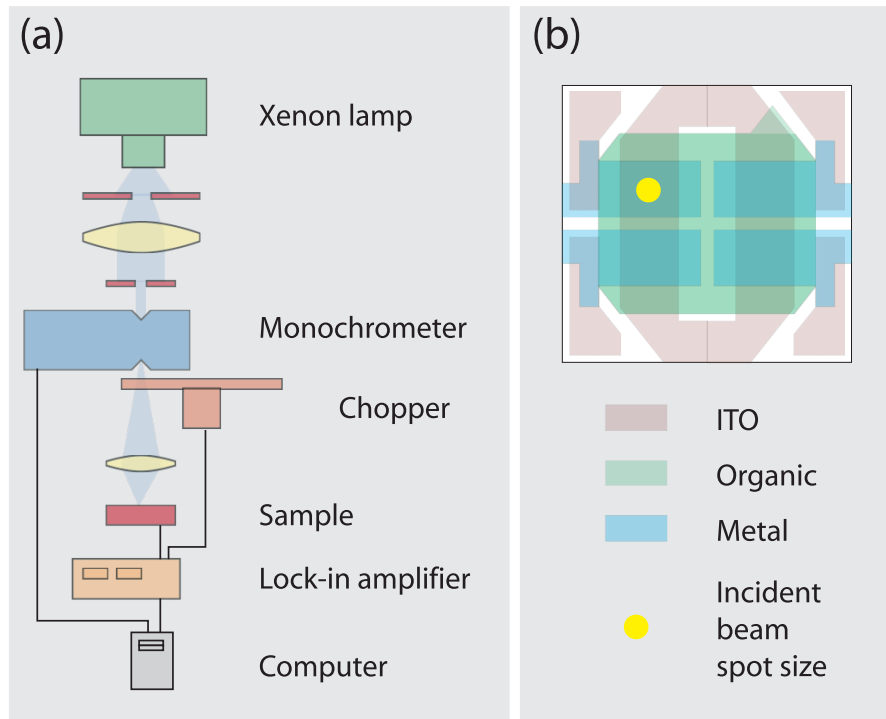


Figure 5-1: Diagram of setup used to measure photocurrent spectra (a) and illustration of incident beam spot size on a pad of the sample device (b).

### 5.1.2 Quantum Efficiency

We calculate quantum efficiency by referencing the sample photocurrent  $I$  to the photocurrent obtained by a calibrated photodiode  $I_r$  with a known responsivity  $R$  at a wavelength  $\lambda$ . Responsivity is defined as

$$R \equiv \frac{I_r}{P}$$

where  $P$  is the incident power and is given by

$$P = \frac{dE}{dt} = \frac{d}{dt} n_{ph} \cdot h\nu = \frac{d}{dt} n_{ph} \cdot h \frac{c}{\lambda} = \frac{hc}{\lambda} \cdot \frac{dn_{ph}}{dt}$$

where  $n_{ph}$  is the number of incident photons,  $h$  is Planck's constant,  $\nu$  is the frequency of light and  $c$  is the speed of light. Solving for  $dn_{ph}/dt$  gives

$$\frac{dn_{ph}}{dt} = \frac{\lambda}{hc} P = \frac{\lambda}{hc} \frac{I_r}{R}$$

The sample photocurrent  $I$  is given by

$$I = \frac{dQ}{dt} = \frac{d}{dt} n_e q = q \frac{dn_e}{dt}$$

where  $n_e$  is the number of photogenerated electrons and  $q$  is the charge of an electron.

Solving for  $dn_e/dt$  gives

$$\frac{dn_e}{dt} = \frac{I}{q}$$

The quantum efficiency % is defined as

$$QE\% = 100 \cdot \frac{n_e}{n_{ph}}$$

Solving for  $n_{ph}$  and differentiating with respect to time gives

$$\frac{dn_{ph}}{dt} = \frac{100}{QE\%} \cdot \frac{dn_e}{dt}$$

Solving for  $QE\%$  and substituting gives

$$QE\% = 100 \cdot \frac{\frac{dn_e}{dt}}{\frac{dn_{ph}}{dt}} = 100 \cdot \frac{\frac{I}{q}}{\frac{\lambda I_r}{hc R}} = 100 \cdot \frac{hc R I}{q \lambda I_r}.$$

Therefore, the quantum efficiency at wavelength  $\lambda$  is then

$$QE\% = 100 \cdot 1240 \cdot \frac{R}{\lambda} \cdot \frac{I}{I_r}.$$

where  $\lambda$  is in nanometers.

## 5.2 Experimental results

In this section, we will show that the photoresponse in the visible can be attributed to charge generation in the quantum dot layer. Additionally, we find that chemical treatment of the quantum dot layer results in an increase in quantum efficiency by over an order of magnitude.

### 5.2.1 Control device without a quantum dot layer

The vacuum evaporated control device with the structure ITO/TiO<sub>2</sub>/TPD/Ag displays no response below the absorption edge of the TPD or TiO<sub>2</sub>, as shown in Figure 5-2. The band gap of both TiO<sub>2</sub> and TPD is roughly 3.2 eV [56]. Beyond the absorption edge, we observe a broad photocurrent peak and it is impossible to distinguish the relative contribution of the TPD or TiO<sub>2</sub> layers.

One might ask why the quantum efficiency is fairly low, given that (a) TiO<sub>2</sub> particles are efficient photoreactors for photocatalysis and (b) TPD is an efficient organic photoconductor for electrophotography. The answer is that photocatalysis and electrophotography rely on the generation and transport of only one charge species, whereas photodetectors depend on the transport of both charge carriers. In the case of a TiO<sub>2</sub> particle in photocatalysis, a photogenerated hole can remain deep in the particle core while the electron travels to the surface in order to participate in oxi-

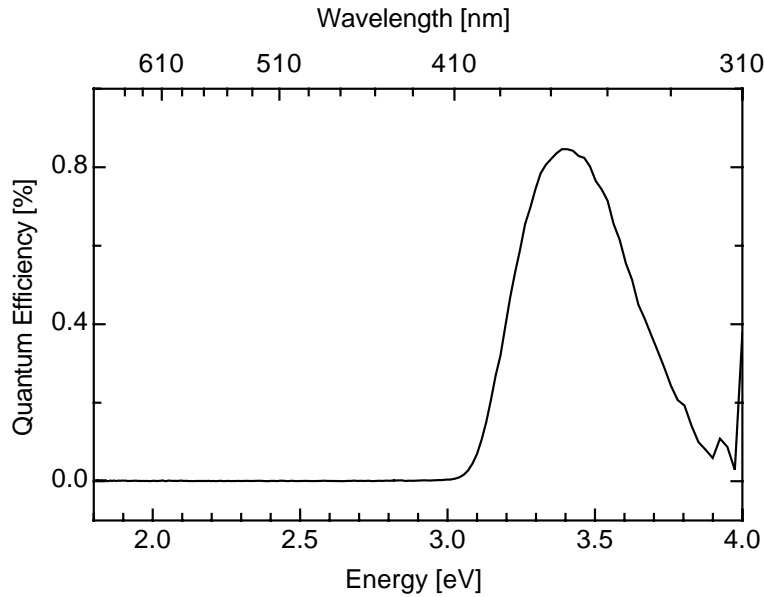


Figure 5-2: Quantum efficiency % versus incident photon energy in eV of an ITO/TiO<sub>2</sub>/TPD/Ag device without a quantum dot layer. The photoresponse above 3 eV is due to photoexcitation in both the TiO<sub>2</sub> film and the TPD film. No signal is observed below 3 eV.

dation. In electrophotography, photo-excited electrons stay trapped in the bulk film while holes can travel and accumulate at the drum surface. But in a heterojunction photodetector, one charge species must cross the heterojunction border while the other must travel the length of the film to the opposite electrode. Usually this occurs according to the sequence of exciton generation, exciton diffusion to the junction interface, dissociation at the interface and then transport of individual carriers to the electrodes.

A number of issues can interrupt the excitonic process. In the bulk, the exciton diffusion distance is limited by dissociation or recombination at traps sites. Often the presence of oxygen will cause trapping and hence a lower quantum efficiency. At the interface, intimate contact between films is necessary in order to promote wavefunction overlap, which leads to efficient transfer of charge. Presently, we have not characterized the morphology of the TiO<sub>2</sub>/TPD interface.

### 5.2.2 Devices with a quantum dot layer

The photocurrent spectra of devices with an untreated CdSe layer (Figure 5-3b) and with a treated CdSe layer (Figure 5-4b) largely mirror the absorption of the CdSe quantum dots. The quantum efficiency of the treated device is greater than the quantum efficiency of the untreated device by over an order of magnitude at the 550 nm absorption peak of the CdSe.

We obtain the absorption of the CdSe film by measuring the transmission of an area of the substrate that is covered only by the CdSe film (Figures 5-3a & 5-4a). The *internal* quantum efficiency is the quantum efficiency divided by the absorption, shown in Figures 5-3c & 5-4c. Note that the Ag back contacts are semitransparent and we were unable to measure their reflection. The internal quantum efficiency is low for both samples.

Compared to previous work by Ginger, et al. [22], the efficiencies presented here are somewhat lower. In a simple ITO/CdSe/Al structure, Ginger observed a 4% quantum efficiency at the first CdSe absorption peak of a 200 nm film with an absorption of 60%, which gives an internal quantum efficiency of around 7%. As we saw in chapter 4, resistive losses in our samples significantly limit the photocurrent, but at these low illumination intensities, resistive losses shouldn't play a significant role. However, the presence of oxygen in the CdSe film may be trapping a large amount of charge in the CdSe film. Additionally, trapped charge is likely to accumulate at the TiO<sub>2</sub> interface, due to the potential barrier of approximately 0.4 eV (Figure 2-8). One way to test if there is a charge transport bottleneck at the TiO<sub>2</sub> interface is to replace the TiO<sub>2</sub> with a higher work function metal oxide like zinc oxide (ZnO) or tin oxide (SnO).

The increase in efficiency with butylamine treatment is consistent with the work by Jarosz, et al. [23] on colloidal CdSe films (see section 2-4). As the CdSe film is compacted by butylamine treatment (from 80 nm to 40 nm), the electronic interaction between neighboring confined states is enhanced somewhat. Thus, we observe a slight 10 nm redshift in the absorption of the CdSe film due to a reduction in wavefunction confinement. This redshift is also reflected in the photocurrent spectrum. It is pos-

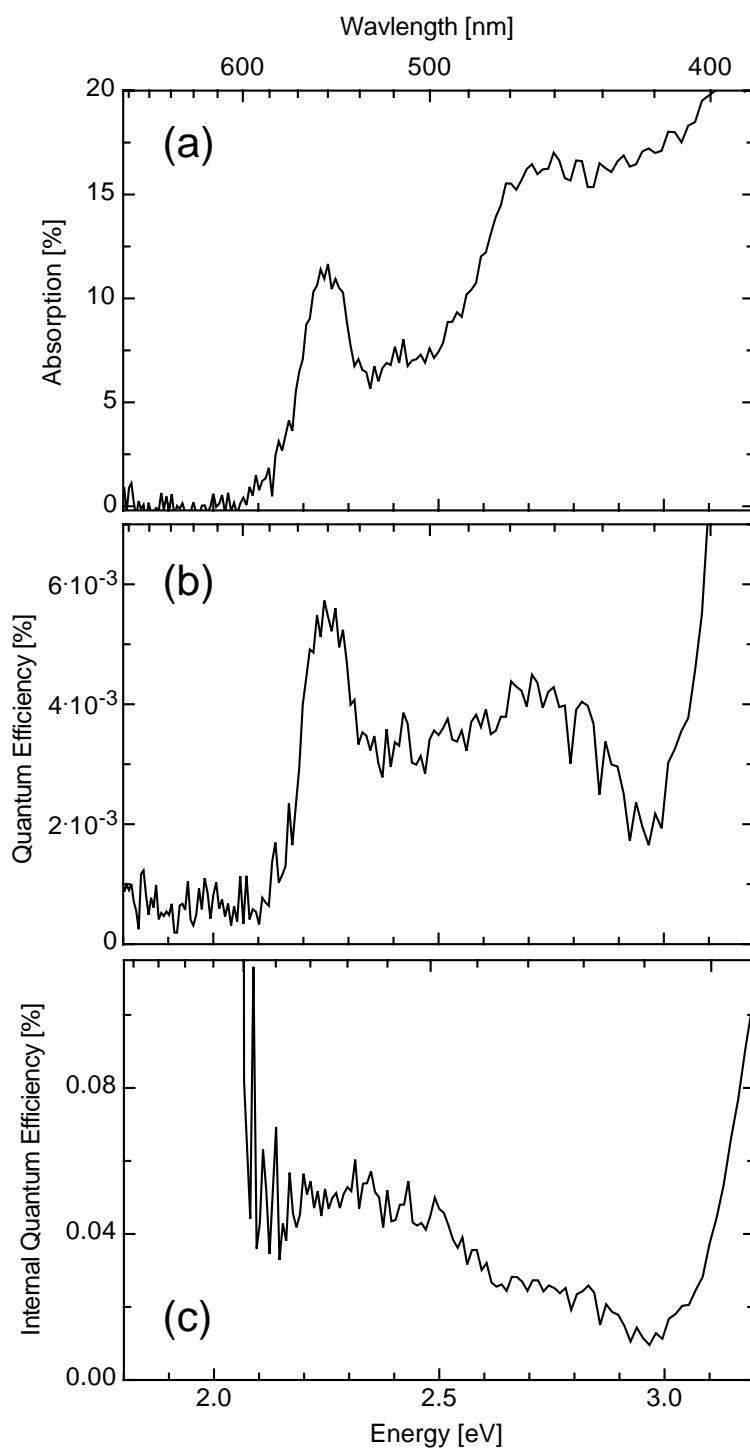


Figure 5-3: Absorption spectrum (a) of an 80 nm CdSe film. The quantum efficiency % (b) of our ITO/TiO<sub>2</sub>/CdSe/TPD/Ag device is weak but measurable. The resulting internal quantum efficiency is low (c).

sible that greater wavefunction overlap results in longer exciton diffusion lengths, in addition to increased conductivity as observed in chapter 4. At this point, we cannot distinguish between the relative contributions of bulk and interfacial dissociation. Nor can we evaluate the effect of butylamine on charge generation via passivation of surface states.

### **5.3 Summary**

We have presented the photocurrent spectra for quantum dot heterojunction photodetectors and a control device without quantum dots. The magnitude of the quantum efficiency is low, but displays distinct spectral traits of the CdSe film. Treatment of the CdSe quantum dot film increases the photocurrent quantum efficiency by over an order of magnitude.



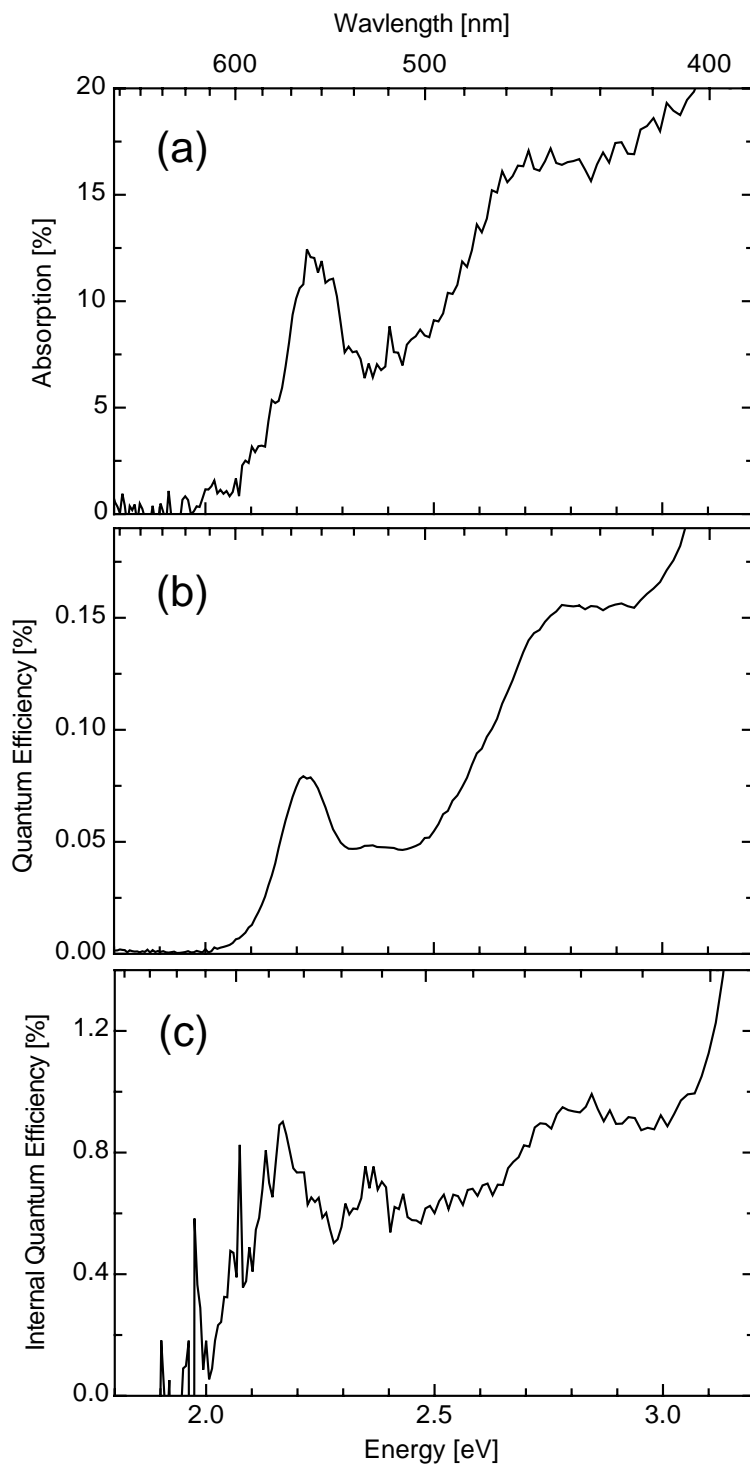


Figure 5-4: Absorption spectrum (a) of a 40 nm treated CdSe film. The quantum efficiency % of an ITO/TiO<sub>2</sub>/CdSe/TPD/Ag device with treated CdSe is significantly higher than that of the previously untreated device. The corresponding internal quantum efficiency (c) is relatively even across the CdSe absorption.



# Chapter 6

## Photocurrent-voltage characteristics

In the previous chapter, we saw how the photocurrent spectrum can help us identify which device layers are photo-active. These measurements were performed at zero bias to ensure that gain doesn't interfere with the determination of quantum efficiency. This chapter will focus on the voltage dependence of the photocurrent signal, using the third of three electrical characterization methods: photocurrent-voltage characteristics. We begin with a description of the experimental apparatus and then present data showing that the photocurrent saturates at around 1V of reverse bias.

### 6.1 Measurement apparatus

All of the device structures that we've studied in this work display a tendency to develop large leakage currents when biased at only moderate (1 or 2 Volts) bias. This complicates i-v measurements at low intensities because the dark current can drown out the current in light. To address this problem, we've built a custom LabView-based program that interfaces the monochromator and lock-in amplifier, and sweeps voltage bias for a particular wavelength. The result is a measurement of the photocurrent versus voltage that is less sensitive to dark current and other noise than regular i-v measurements.

### 6.1.1 Description of measurement

This measurement is similar to photocurrent spectra, except that a Keithley 2400 source-measure unit is connected to the positive lead of the sample (Figure 6-1). The response time of the 2400 is  $30\ \mu\text{s}$ , much less than the chopping period used (usually around 45 Hz, 22 ms). First, a wavelength is specified and the monochromator is set. Then the Keithley applies a voltage to the sample and waits one second for the lock-in to settle and another 0.5 seconds while the lock-in takes a current reading. This process repeats until a full voltage scan is completed.

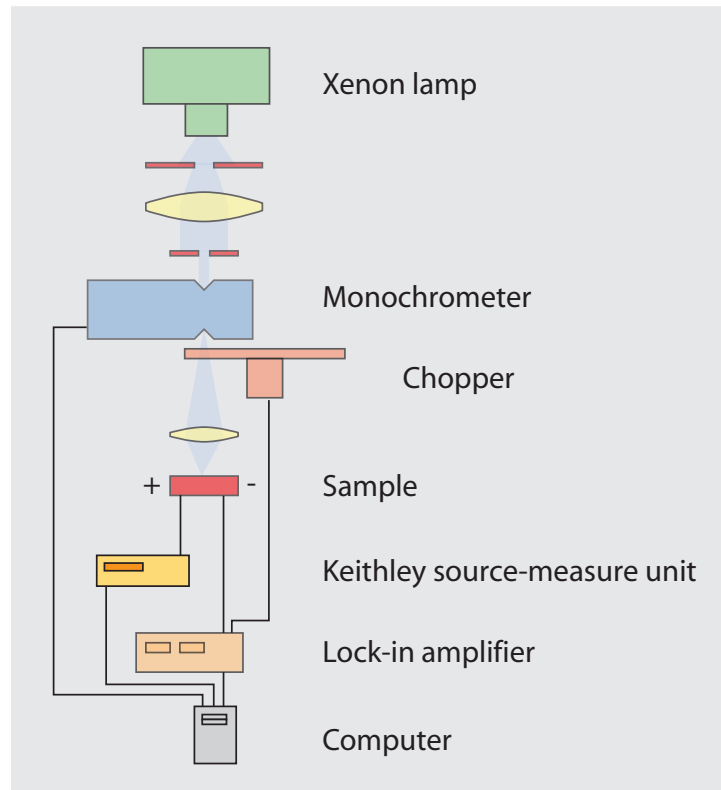


Figure 6-1: Diagram of setup used to measure photocurrent-voltage characteristics.

## 6.2 Experimental results and discussion

In this section, we will show that the photocurrent saturates at around 1 Volt. Additionally, we find evidence that charge is being trapped in the quantum dot layer.

In figure 6-2, we plot the photocurrent versus voltage of the ITO/TiO<sub>2</sub>/CdSe/TPD/Ag device with a treated CdSe layer. The photocurrent is given as the *response*, which is essentially equal to the external quantum efficiency, but contains an important distinction. The term *quantum efficiency* - the number of electrons generated *in the device* per incident photon - is reserved for photocurrent measured at zero bias. In contrast, we define the response as the number of electrons flowing *through the device* per incident photon, aided by the application of voltage. This distinction is relevant when the photocurrent gain is greater than 1. In this case, under applied voltage, the number of generated electrons is not equal to the number of electrons flowing through the device.

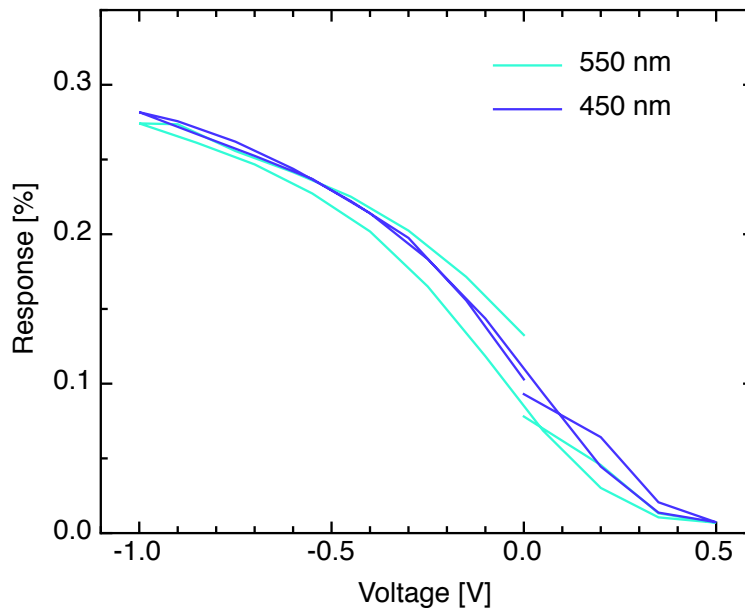


Figure 6-2: Response % of the ITO/TiO<sub>2</sub>/CdSe/TPD/Ag treated device, illuminated at 450 nm and 550 nm.

Figure 6-2 shows the response at two different wavelengths, 550 nm (the first absorption peak of CdSe) and 450 nm. The response is voltage dependent and falls

to zero at 0.5 V, the built in voltage of the device. The voltage dependence can be attributed to either field-dependent dissociation, a large series resistance, a low shunt resistance, or a strongly field-dependent injection current. From our analysis of the i-v characteristic in chapter 4, we know that injection current is blocked by the TiO<sub>2</sub> and TPD transport layers. We also know that a large series resistance is present. Because of this series resistance, we cannot distinguish between field-dependent or field-independent dissociation.

Scanning to greater negative bias, as shown in Figure 6-3, reveals three important qualities of the device. First, beyond a voltage of -1V, the photocurrent saturates sharply. Second, a reversible hysteresis develops when saturation is reached. And third, repeated scans yield lower and lower current values.

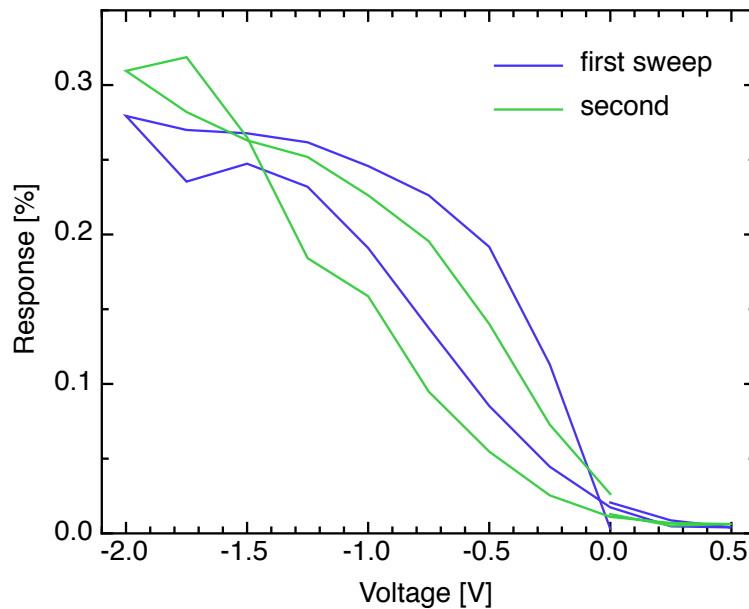


Figure 6-3: Scanning to higher voltages reveals saturation of the photocurrent response %. Illumination is at 550 nm. Both hysteresis and noise due to device instability at higher voltages are apparent.

Photocurrent saturation occurs when field-independent charge generating mechanisms become dominant. For instance, the total number of photoexcited electron-hole pairs is field-independent, whereas transport through a highly resistive layer is field-dependent. We can interpret the saturation as a transition from Ohmic transport to

a carrier-limited regime. The electric field at which saturation occurs is comparable to that observed by Jarosz [23] in a planar device structure (described in section 2-4). Assuming that the CdSe film is highly resistive, most of the applied voltage will be dropped across this layer, leaving a lesser field drop across the TiO<sub>2</sub> and TPD films. For a 40 nm CdSe film, the electric field is  $4 \times 10^7$  V/m (considering a -1V applied bias and -0.5V of built in bias), compared to a saturation field of  $6 \times 10^7$  obtained by Jarosz.

The magnitude of the saturation current is influenced by trapped charge at the interface between CdSe and TiO<sub>2</sub>. Electrons that have accumulated at the interface cannot tunnel into the TiO<sub>2</sub> layer unless a significant field (on the order of  $10^8$  V/m) is applied across the TiO<sub>2</sub>. However, the field across the TiO<sub>2</sub> layer is likely to be several orders of magnitude smaller, since the n-doped TiO<sub>2</sub> layer is expected to be several orders of magnitude more conductive than the intrinsic CdSe layer. In this case, the percentage of electrons that can inject into the TiO<sub>2</sub> film is determined solely by thermal excitation over the potential barrier, which is independent of bias voltage. The potential barrier at the TiO<sub>2</sub>/CdSe interface also effects exciton dissociation. Excitons generated in the CdSe layer that diffuse to the TiO<sub>2</sub>/CdSe interface can exist only briefly before recombining. The large potential barrier forces longer residence times at the interface, resulting in a lower dissociation efficiency.

To get a sense for the reduction in efficiency associated with electron trapping, we can compare the extraction efficiency of electron-hole pairs generated in the TPD in the control device (Figure 6-4) versus the extraction efficiency of electron-hole pairs generated in the TPD in the device with a CdSe layer (Figure 6-5). The efficiency drops from 5% to 2.5% when the CdSe layer is inserted. This factor of two, however, does not completely account for the low quantum efficiency observed when exciting charge in the CdSe layer. Even considering 10% absorption in the CdSe film, the internal quantum efficiency saturates at only around 3%. Multiplying by a factor of two would bring the internal quantum efficiency up to the levels observed by Ginger [22] (around 7%), but is still below the quantum efficiency of bulk inorganic photodetectors, which is around 90%.

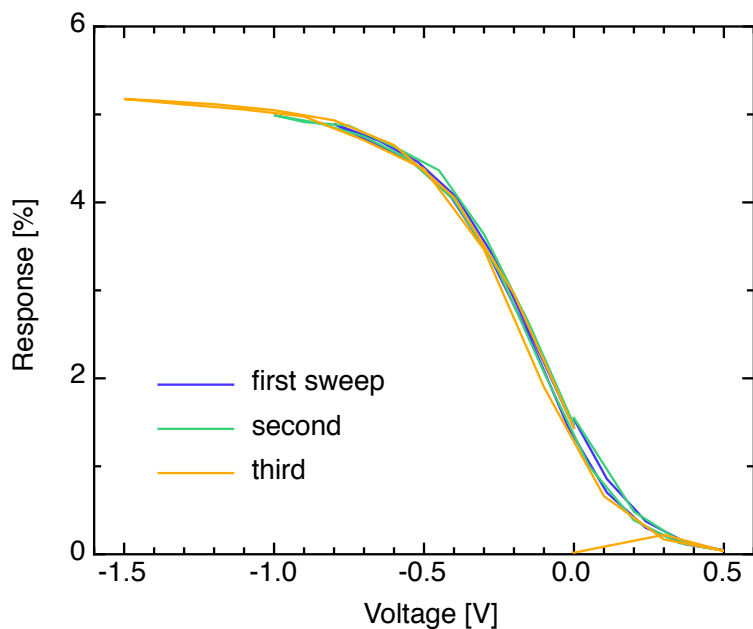


Figure 6-4: Response % versus voltage of an ITO/TiO<sub>2</sub>/TPD/Ag device without a quantum dot layer. The sweep was repeated several times with no degradation.

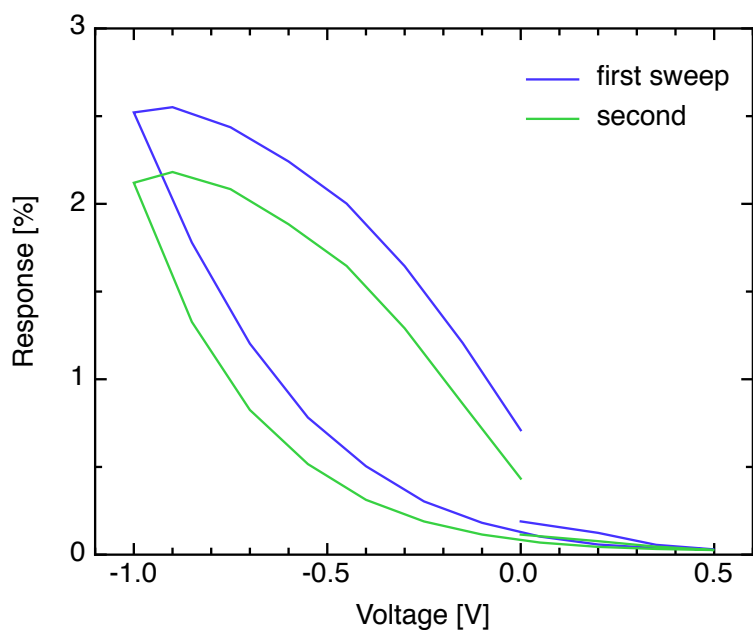


Figure 6-5: Response % at 360 nm shows saturation, hysteresis and signal degradation between sweeps.



Further evidence that the photocurrent signal is dominated by trapped charge is given by the strong hysteresis observed in all samples containing a quantum dot layer. When scanning from negative bias upward, the photocurrent drops off precipitously and flattens out as the voltage approaches zero. Note that we have repeated this procedure by hand with long wait times between voltage steps and obtained identical results. Hysteresis is also observed when exciting only the TPD film (Figure 6-5) in devices containing the CdSe layer, which implies trapping of electrons as they pass through the CdSe layer on their way to the TiO<sub>2</sub> film. No hysteresis is observed in the control device without a CdSe layer (Figure 6-4).

Devices containing the CdSe layer also exhibited a decaying signal from scan to scan that did not seem to recover with time. We speculate that the CdSe layer is experiencing oxidization. The i-v measurements taken under nitrogen (described in chapter 4) did not show any form of degradation. Further measurements are needed in order to characterize the effect of oxygen on the charge generation efficiency.

### **6.3 Summary**

We have presented photocurrent versus voltage measurements for a photodetector with and without a quantum dot layer. We observe photocurrent saturation at an applied bias of -1V. Hysteresis is present in devices containing a quantum dot layer, but absent in devices without a quantum dot layer. We propose that the hysteresis and low quantum efficiencies are due, to some extent, to trapped charge at the CdSe/TiO<sub>2</sub> interface.



# Chapter 7

## Conclusion

This thesis has explored the use of colloidal quantum dots in a novel heterojunction photodetector. The photodetector, consisting of a solution processed layer of CdSe quantum dots sandwiched between TiO<sub>2</sub> and TPD, is the first colloidally-grown quantum dot based device to exhibit low dark current in reverse bias, an essential feature of high performance photodetectors.

From current-voltage measurements, we have identified high internal resistance of the CdSe film as a major limitation to device performance. We found that treatment with butylamine improves the film conductivity, but further work is needed to either (a) reduce the resistance of CdSe films or (b) fabricate high surface area structures that can accommodate ultra-thin CdSe films. From photocurrent spectra, the quantum efficiency of the device is found to be slightly lower than that reported by other groups. We suspect that trapping at the TiO<sub>2</sub>/CdSe interface is interfering with the charge separation process. Under applied bias, we found that the photocurrent signal saturates in reverse bias, which is consistent with charge blocking at both electrode interfaces. We also observed strong hysteresis when scanning the applied voltage, which is consistent with trapped charge in the CdSe layer. In order to reduce trapping in the CdSe film, future device designs should use an alternative electron transport layer with a larger electron affinity, thus reducing the potential barrier at the quantum dot/electron transport layer interface. Zinc oxide (ZnO) or tin oxide (SnO) are good candidates.

The idea of surrounding a quantum dot film with wide-band-gap amorphous semi-conducting contact layers in order to achieve superior device characteristics is widely applicable to other photosensitive material genres, such as organic small molecules, conjugated polymers, j-aggregates and biological photosystems. Without the need for expensive epitaxial techniques, device structures of this sort could lead to inexpensive, large area and efficient photodetection or light harvesting systems.

# Appendix A

## Procedure for patterning ITO-glass substrates

This document describes the procedure developed by John Kymissis for photolithographically patterning ITO-coated glass substrates, beginning with large 13" x 13" ITO-glass sheets. Following this procedure results in  $4\frac{2}{3}$ " x  $4\frac{2}{3}$ " patterned ITO glass slides that can then be cut into one inch or half inch substrates with the dicing saw. The  $4\frac{2}{3}$ " glass fits perfectly into our 170 x 90 mm pyrex crystallization dishes, which is useful when etching the ITO and stripping off the resist film. The 13" x 13" ITO-glass sheets and pyrex beakers are generally kept in the cabinet in the instrument room.

### A.1 Supplies

- 13" x 13" ITO-glass sheet
- Diamond scribe
- 2 containers suitable for developing resist
- Acid-resistant wafer tweezers
- Sodium carbonate
- 2 170 x 90 mm pyrex crystallization dishes

- ITO etchant
- Hot plate
- Butyl gloves
- Face shield
- Isopropanol
- Ohmmeter

## A.2 Procedure

1. Cut 13" x 13" sheets to size
  - (a) Roughly measure out and mark  $4\frac{2}{3}$ " x  $4\frac{2}{3}$ " sized pieces
  - (b) Scribe and break by hand
2. Pre-clean ITO-glass
  - (a) Wipe with texwipe wetted with 2% micro90 in H<sub>2</sub>O
  - (b) Rinse with H<sub>2</sub>O and then with isopropanol
  - (c) Blow dry
  - (d) UV-ozone for 5 minutes
3. Lamination
  - (a) Mark ITO side
  - (b) Turn on laminator and set temperature to 110C at speed = 1
  - (c) Wait until roller is heated (display with say "ready") and press "run" to laminate
  - (d) Cut sample out of film, leave 1 cm margin around edge
4. Exposure and development
  - (a) Mix up developer: 1% sodium carbonate in H<sub>2</sub>O (10 g in 1l)
  - (b) Fill second tank with H<sub>2</sub>O
  - (c) Place sample in drawer, safe from UV exposure
  - (d) Set exposure to 14 units on the photolith machine
  - (e) Press start and leave room until UV lamp is extinguished

- (f) Place sample under glass plate and apply vacuum
- (g) Expose samples
- (h) Cut top film around edge of sample
- (i) Remove top and bottom films, leaving middle resist layer
- (j) Develop in sodium carbonate bath until reflection of room lights can be seen in developed areas
- (k) Rinse in H<sub>2</sub>O when developed
- (l) Dispose of developer in the drain and rinse containers

#### 5. Etching

- (a) Using butyl gloves and face shield, fill pyrex dish with stock ITO bath
- (b) Apply medium heat (setting = 3)
- (c) Etch sample for 15 minutes
- (d) Remove with acid resistant tweezers and rinse with water in fume hood sink
- (e) Blow dry and test conductivity of etched ITO regions
- (f) Carefully pour ITO etch into a large beaker using a funnel and then pour etch back into its original jar using funnel
- (g) Thoroughly rinse pyrex dish, let dry and return dish to instrument room

#### 6. Stripping

- (a) Fill the other pyrex dish with isopropanol
- (b) Strip remaining photoresist
- (c) Rinse pyrex dish with isopropanol, let dry and return dish to instrument room





# Appendix B

## Procedure for cutting patterned ITO-glass using the dicing saw

This document describes the procedure for cutting half inch substrates out of a  $4\frac{2}{3}$ " x  $4\frac{2}{3}$ " piece of patterned ITO glass. Most supplies are located in the second from the top cabinet drawer closest to the dicing saw. The wafer-mounting film is located in the larger cabinet drawer and should be kept wrapped in black plastic to minimize UV exposure. To release substrates from the mounting film after cutting, place under UV lamp for 20 minutes. Consult the dicing saw manual located next to the saw for more detailed information. Please wear eye protection when operating the saw.

### B.1 Supplies

- Wafer-mounting film
- Razor blade
- Scrap piece of ITO-glass
- Dicing saw blades suitable for cutting glass
- Adjustable wrench
- Allen wrench 5/16"
- Tweezers

- 3 pinned blade holder disassembly tool
- Ohmmeter
- Eye protection

## B.2 Procedure

1. Laminate glass sample to wafer-mounting film
  - (a) Cut out segment of mounting film
  - (b) Tear end to separate plastic backing film from adhesive layer
  - (c) Place adhesive layer face up on counter
  - (d) Hold glass, ITO side up, at a 45° angle above the film
  - (e) Press the glass onto the film and slowly slide both over the edge of the counter, applying pressure at the counter edge where the glass and film intersect
  - (f) Avoid air bubbles between the glass and film
  - (g) Trim film with razor as close as possible to the edge of the glass
2. Inspect saw
  - (a) Consult log book to see if a Si or glass blade is installed.
  - (b) Always remove plastic safety window and inspect blade, regardless of whether you need to change the blade or not. Check to ensure that the blade is not broken and that the holding nut is secure.
3. Change blade
  - (a) Unscrew the holding nut with an adjustable wrench by turning the shaft with a hex wrench.
  - (b) Remove washer
  - (c) Use blade removal wand to extract blade holder piece
    - i. Turn on vacuum pump
    - ii. Turn on vacuum to blade removal wand by flipping switch under front left side of dicing saw
    - iii. Place wand flush against saw holder piece and pull out saw holder piece
    - iv. Turn off vacuum to wand
    - v. Turn off vacuum pump

- (d) Open blade holder piece with 3 pin tool
- (e) Remove blade with tweezers, replace, reassemble holder piece, remount onto shaft, remount washer, tighten nut and fasten window

4. Programing dicing saw

- (a) Press and turn “Stop” button to turn on dicing saw
- (b) Press “Program,” chose a parameter, enter value given in the table below and press “Enter.” Units are in Mils

Parameter	Description	Value
Mode	substrate shape and cutting sequence	30
1st Index	length between cuts in y-direction	495
2nd Index	length between cuts in x-direction	495
Height	thickness of mounting film	3
Thickness	thickness of substrate	46.5
Angle	angle between cutting directions	90
Speed	Mils/sec	500
*	substrate dimension in y-direction	4666
Dia	substrate dimension in x-direction	4666

- (c) Press “Reset”

5. Start saw

- (a) Turn on vacuum pump
- (b) Turn on nitrogen until resistance on multimeter drops
- (c) Press “Spindle” to start saw

6. Zero chuck

- (a) Put metal gauge disk on chuck
- (b) Press “Lock” to turn on vacuum to chuck
- (c) Press “Chuck Zero”
- (d) Press “Unlock” to release vacuum
- (e) Remove gauge disk

7. Make a test cut for reference

- (a) Laminate mounting film to a test piece of ITO glass
  - (b) Place test sample on chuck and press “Lock”
  - (c) Press “Align” and “Single Cut” to make one test cut down middle of sample
  - (d) Turn on monitor
  - (e) Move horizontal reference line on screen to center of previous cut by pressing “up” or “down” on side of camera housing.
  - (f) Press “Fast” and “Left” to move chuck away from blade
  - (g) Press “Unlock” and remove test sample
8. Align and cut substrates
- (a) Mount new sample
  - (b) Align patterned markers on substrate with reference line on monitor
  - (c) Press “Autocut” to automatically cut all streets and then rotate chuck by  $90^\circ$
  - (d) Repeat alignment and press “Autocut”
9. Remove sample and shut down system
- (a) Press “Standby” to stop saw
  - (b) Press “Unlock” and remove sample
  - (c) Turn off vacuum pump
  - (d) Turn off nitrogen
  - (e) Turn off monitor
  - (f) Press “Stop” to turn off system

# Appendix C

## Procedure for solgel deposition of TiO<sub>2</sub> films

This document describes the procedure for preparing thin (100 nm) films of titanium dioxide (TiO<sub>2</sub>) from a liquid titanium ethoxide solgel, a TiO<sub>2</sub> precursor. Films are spin deposited and then heated at 500C for 30 min in order to convert the precursor into TiO<sub>2</sub> and sinter the resulting grains (Figure 3-1).

Note that the solgel cross-links in the presence of water. With time, the solution becomes cloudy and too viscous to spin crack-free films. Stabilizing the solution with hydrochloric acid (HCL) can make it last up to a week, but be aware that films spun at the same speed will become thicker over the course of time.

Once the TiO<sub>2</sub> films have been sintered, they should be transferred to the glove box before cooling below 100C in order to prevent water from adsorbing on the surface.

### C.1 Hazards

Titanium ethoxide oxidizes easily and is highly flammable. Care should be taken to use it only in the right glove box or under a fume hood. Our main supply jar should not be removed from the right glove box.

HCL is a strong acid that can seriously burn your skin. Always wear black butyl gloves, a protective face mask, lab gown and pants. In case of contact with skin,

rinse thoroughly with water and seek medical attention immediately. If clothing is splashed with HCL, remove it immediately. HCL can be disposed of in the drain with plenty of water. Never add water to a container of acid.

## C.2 Supplies

- Titanium ethoxide
- Patterned ITO substrates
- Ethyl-alcohol
- Hydrochloric acid (HCL)
- 2 110 ml beakers
- 1 20 ml vial ?
- glass pipettor
- 1  $\mu$ l micropipettor
- 3 1ml syringes and needles
- 1 10ml syringe
- Stir bar
- Large 4' quartz purification tube
- 1' quartz tube

## C.3 Procedure

1. Make ethanol solution
  - (a) Pour 20 ml or so of ethanol into a 110 ml beaker
  - (b) Transfer 10 ml of ethanol into the 20 ml vial and add stir bar
  - (c) Pour a couple of milliliters of H<sub>2</sub>O into a 100 ml beaker
  - (d) Add 0.25 ml of H<sub>2</sub>O to vial of ethanol
2. Add HCL to solution
  - (a) Prepare glass pipetter

- (b) Put on butyl gloves and face mask
  - (c) Add 10 drops of concentrated (36-38%) HCL to ethanol solution
3. Add precursor to solution
- (a) Transfer a 1 ml syringe, an empty 10 ml vial and needle into the right glove box
  - (b) Transfer 1.5 ml of ti-ethoxide to empty vial and remove from glove box
  - (c) With micropipettor, add 1 ml of ti-ethoxide to stirring ethanol solution
4. Heat solution
- (a) Set temperature on hot plate to 33C, corresponding to 60C
  - (b) Heat for a half hour
5. Prepare ITO-glass sildes
- (a) Clean ITO-glass slide
  - (b) UV-ozone for 5 min
  - (c) Mask edges of slide with Scotch tape under laminar flow hood
6. Spin TiO<sub>2</sub> film
- (a) Set spinner to 2000 rpm for 30 secs, ramp rate of 10,000
  - (b) Set micropipettor to 100  $\mu$ l for half inch slide and 200  $\mu$ l one inch slide
  - (c) Place sample on spinning chuck and activate vacuum
  - (d) Deposit solgel and spin
  - (e) Active vacuum and remove scotch tape with substrate on chuck
  - (f) Release vacuum and remove substrate
7. Transfer slides to tube oven
- (a) Under laminar flow hood, place slide in 1' quartz tube
  - (b) In purification room, place 1' quartz tube in large purification tube
8. Attach purification tube to tube holder apparatus
- (a) Open tube oven and place purification tube on fiberglass interior
  - (b) Clean around end of purification tube, inside tube holder apparatus and inside assembly parts with isopropanol and a labwipe
  - (c) Slide compression seal nut, then compression ring and then the o-ring onto the purification tube
  - (d) Slide tube into tube holder apparatus

- (e) Bring o-ring flush with edge of tube holder and screw in compression seal nut while keeping tube perfectly horizontal
9. Pump down purification tube
    - (a) Close vent valve
    - (b) Open valve to roughing pump, making sure that the valve to other purification system is closed
    - (c) Close tube oven
    - (d) Wrap Aluminum foil around oven opening on Zone 1 side to keep heat in
  10. Fire TiO<sub>2</sub> film in tube oven
    - (a) Set tube oven to 500C and wait approx 1 hour until temperature reaches 500C
    - (b) Allow slide to bake at 500C for 30 minutes
  11. Shut down system
    - (a) Press black power switch to turn heat off and wait until temperature cools to around 200C
    - (b) Close backing valve
    - (c) Open vent valve slowly to vent the tube
  12. Remove samples from oven
    - (a) Using insulated gloves, unscrew tube from holder
    - (b) Tilt tube slightly, open end down, and gently tap on end of tube to slide out insert tube
    - (c) Place insert tube directly into glove box, taking care not to let substrates cool below 100C while exposed to air



# Appendix D

## Procedure for purification of organic materials

This document describes the procedure developed by Debbie Mascaro for purifying organic small molecule powders by thermal gradient sublimation. Following this procedure results in high-purity organic material suitable for device manufacture. We use a turbo pump to maintain high vacuum inside a quartz purification tube (Figure 3-4). The tube is heated by a tube oven capable of applying a temperature gradient across the tube.

High-purity material is obtained in the following way. The organic source material is heated above its sublimation temperature in Zone 1 and is deposited in Zone 2 where the temperature is kept below the sublimation temperature. Residual impurities remain in Zone 1 and volatile impurities collect in Zone 3, which is kept at a temperature well below that of Zone 2. The high-purity organic can be collected off the sidewalls of the quartz insert tube with a clean spatula.

The large 4' quartz purification tubes are stored in the fume hood in the Chemistry lab. Clean insert tubes are stored in the third drawer under the tube oven. Spatulas are located in the drawer under the tube oven. To prevent cross contamination, they are to be used with only one material and are labeled accordingly. Always clean spatulas before and after use and wrap in Aluminum foil when done.

Each purification setup has a log book. You must make an entry if you use the

system for any purpose. Consult past entries in the log book to determine which temperature profile to use for your material.

## D.1 Hazards









Adverse health effects of some organic materials have not been fully evaluated. Always handle organic powders under a fume hood. Wear gloves when operating tube oven, which may be contaminated with organics. Store used purification tubes under the fume hood in the Chemistry lab.

## D.2 Supplies

- Spatula
- 4' quartz tube, rounded on one end
- 3 1' quartz tubes
- 2 6" quartz tubes, rounded on one end
- Quartz wool
- Aluminum foil

## D.3 Procedure

1. Assemble quartz tubes
  - (a) Place quartz tubes and source material in fume hood
  - (b) Clean the spatula
  - (c) Transfer approximately 5 grams of the source material into one of the 6" insert tubes
  - (d) Clean the spatula
  - (e) Place insert tubes inside large tube one by one, sliding each in carefully
  - (f) Cover end of 4' tube
2. Attach purification tube to tube holder apparatus
  - (a) Open tube oven and place purification tube on fiberglass interior

- (b) Clean around end of purification tube, inside tube holder apparatus and inside assembly parts with isopropanol and a labwipe
  - (c) Slide the compression seal nut, then the compression ring and then the o-ring onto the purification tube
  - (d) Slide tube into tube holder apparatus
  - (e) Bring o-ring flush with edge of tube holder and screw in the compression seal nut while keeping tube perfectly horizontal
3. Pump down purification tube
- (a) Close vent valve
  - (b) Open valve to roughing pump, making sure that the valve to other purification system is closed
  - (c) Wait for pressure to drop below 0.1 Torr (you may have to tighten the compression seal nut further)
  - (d) Turn on turbo pump
  - (e) Close tube oven
  - (f) Wrap Aluminum foil around oven opening on Zone 1 side to keep heat in
4. Set ramp rate and temperature for each zone on tube oven
- (a) Press  until screen shows “SPrr” and input ramp rate
  - (b) Press  and  to set ramp rate
  - (c) Press  again until screen shows “Stat”
  - (d) Press  to change temperature ramp status from “off” to “run”
  - (e) Press  to finish programming
  - (f) Press  and  to set temperature
  - (g) Press black power switch to turn heat on
  - (h) Wait around 8 hours for oven to reach target temperature and for material to migrate toward Zone 2
5. Shut down system
- (a) Press black power switch to turn heat off and wait until temperature cools to room temperature
  - (b) Turn off turbo pump, close backing valve and wait until turbo spins down
  - (c) Open vent valve to vent the tube
  - (d) Unscrew tube from holder

- (e) Place tube in fume hood
6. Collect purified material
- (a) Tilt tube slightly, open end down, and gently tap on end of tube to slide out insert tubes
  - (b) Clean spatula
  - (c) Scrape out purified material and place tube in base bath
  - (d) Clean spatula
  - (e) Clean out residual impurities from first 6" tube and place tube in base bath
  - (f) Place other insert tubes that are excessively dirty in base bath, otherwise re-insert tubes into 4' tube and store in fume hood in the Chemistry lab.

# Appendix E

## Procedure for measuring current-voltage characteristics under illumination

This document describes the procedure for measuring current-voltage characteristics using the computer controlled HP 4146B setup in room 26-444. Following this procedure results in a measurement of current-voltage curves in dark and at various illumination intensities.

### E.1 Calibration

To roughly characterize the light intensity incident on your sample, use a Newport 818-UV photodiode with an OD 3 filter. The responsivity of the photodiode with filter attached is  $3.5 \times 10^{-4}$  A/W across almost all of the lamp emission spectrum. The surface area of the detector is  $1 \text{ cm}^2$ . Placing the detector surface nearly an inch away from the light source gives the following approximate intensities:

Voltage (V)	Intensity (mW/cm <sup>2</sup> )
0	-
2	0.1
4	2
6	8
8	20
10	30
12	48

## E.2 Apparatus

- HP Semiconductor Parameter Analyzer 4145B
- Agilent E3615A DC power supply 0-20V 0-3A
- Xenon bulb and housing
- LabView program “ivmeasure6.vi”

## E.3 Procedure

1. Connect HP to rear panel of DC power supply (Figure E-1)
  - (a) Connect the positive lead of VS1 to the connection labeled +CV
  - (b) Connect VS1 ground to the connection labeled -CV
  - (c) Flip CV switch to remote setting
2. Turn on equipment
  - (a) Turn on HP 4145B
  - (b) Turn on DC power supply
  - (c) Open “Shortcut to ivmeasure6.vi” located on the desktop
3. Connect sample and Xenon lamp
  - (a) Connect SMU 2 to sample high
  - (b) Connect SMU 3 to sample ground
  - (c) Connect DC power supply output to Xenon lamp

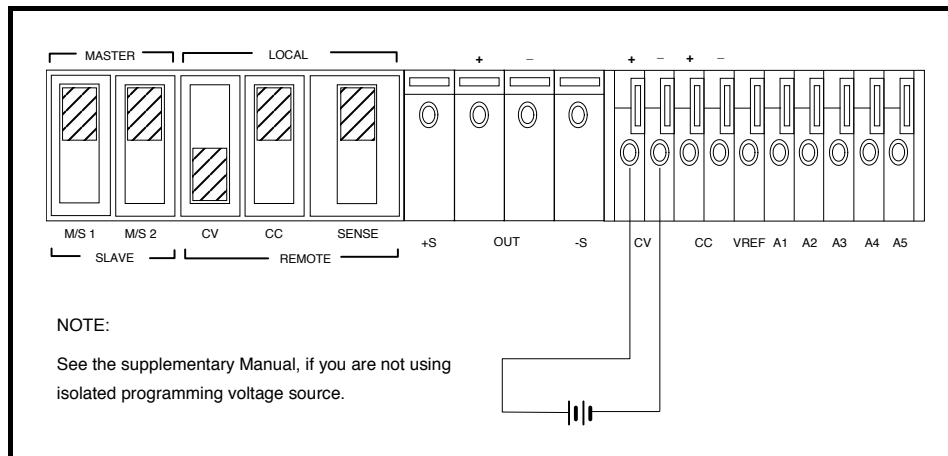


Figure E-1: DC power supply rear panel connections and settings

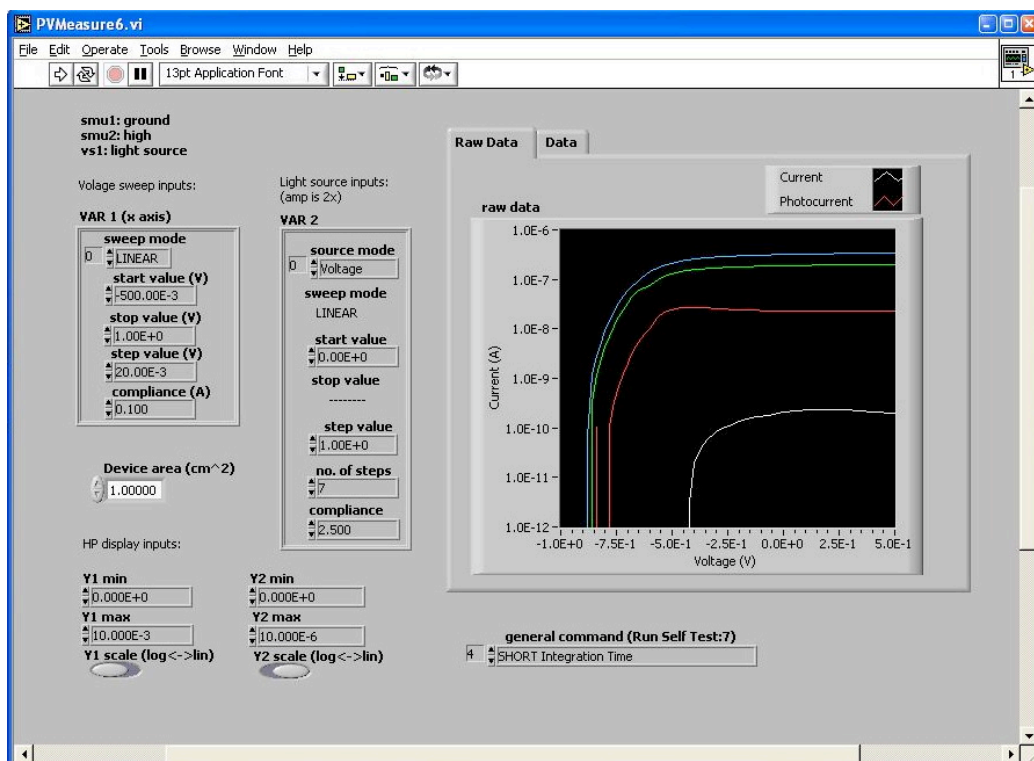


Figure E-2: Front panel of “ivmeasure6.vi”

4. Take measurement (Figure E-2)
  - (a) Configure measurement parameters
  - (b) Press play
5. Save and print data (Figure E-3)

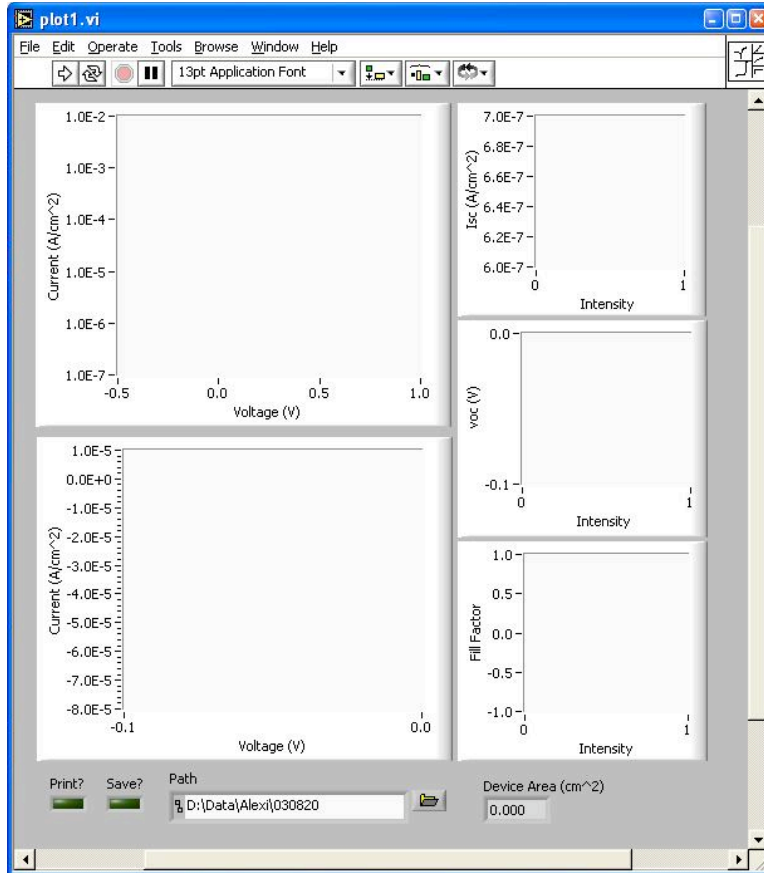


Figure E-3: Data is displayed in a new window

- (a) Enter filename and path
- (b) Click "Print?" and "Save?" buttons
- (c) Press play



# Appendix F

## Procedure for measuring photocurrent spectra

This document describes the procedure for measuring photocurrent action spectra in the visible range of the electromagnetic spectrum using the computer controlled photocurrent setup located in room 26-444. Following this procedure results in a measurement of quantum efficiency versus wavelength.

The monochromator wavelength is controlled by the laptop via the RS232 port since the GPIB interface is unfortunately not functional. Still, the RS232 communication is not perfect. When opening the Labview software that runs the monochromator, “gotowavers232.vi,” it is necessary to run it once, press stop and then run it again. The lock-in is interfaced to the laptop via GPIB.

### F.1 Cautions

Care should be taken to avoid overloading the lock-in. If the input signal is much greater than the scale setting, the lock-in can be damaged. Always set the lock-in input scale to a low sensitivity (high current) setting before connecting any device and then step down the scale to the appropriate value. Always leave the lock-in at the lowest sensitivity setting.

The lifetime of the Xenon lamp is finite, so do not leave the lamp on unused for

long time periods. On the other hand, the lamp lifetime decreases with every power on, so try to minimize power on/off cycles.

## F.2 Apparatus

- Oriel Instruments Xenon arc lamp
- Oriel Instruments Cornerstone monochromator 1/8 m 74000
- Stanford Research Systems SR540 chopper
- 2 lenses
- Newport photodiode 818-UV
- Stanford Research Systems SR830 DSP lock-in amplifier
- LabView program “gotowavers232.vi”
- LabView program “photocurrlockin3.vi”

## F.3 Procedure

1. Turn on lamp
  - (a) Press power on button
  - (b) Press lamp on button
  - (c) Set wattage to 150 W
  - (d) Wait half an hour for lamp to stabilize
2. Turn on chopper
  - (a) Flip power on switch located on the back right side of the chopper
  - (b) Connect the chopper BNC output to the lock-in reference channel
  - (c) Tune the chopper frequency
3. Turn on monochromator
  - (a) Attach the RS232 cable to monochromator and laptop
  - (b) Press power on button
  - (c) Set the input and output apertures to desired widths

4. Set wavelength with laptop

- (a) Open LabView program “Shortcut to gotowavers232.vi” located on the desktop (Figure F-1)

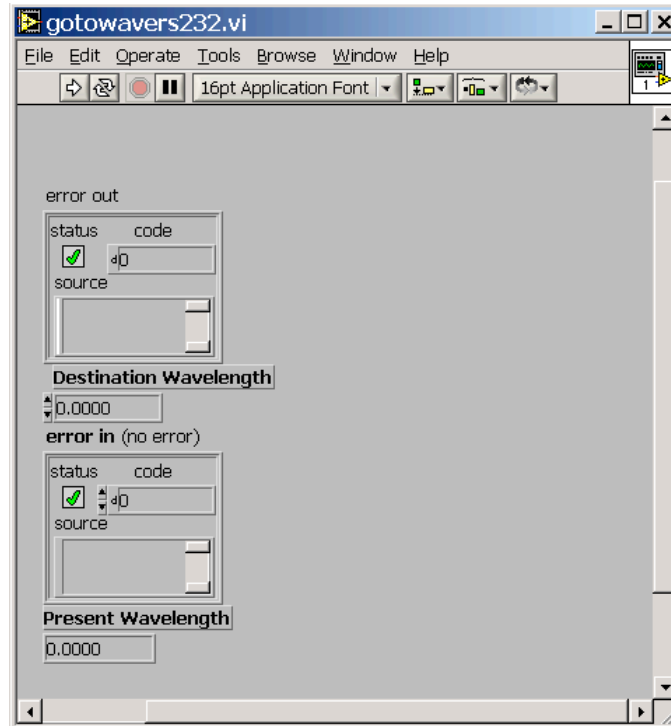


Figure F-1: LabView program “gotowavers232.vi” is used to set the wavelength of the monochromator

- (b) Set the destination wavelength to 475 nm (the wavelength at which the intensity is greatest) and press play
5. Mount reference photodiode
- (a) Place reference photodiode at focal point of incident beam
  - (b) Set scale on lock-in to highest (least sensitive) setting by pressing up arrow repeatedly
  - (c) Connect photodiode BNC to lock-in channel A
  - (d) Set scale on lock-in appropriate to signal
6. Take calibration spectrum
- (a) Set scale on lock-in
  - (b) Open LabView program “Shortcut to photocurrlockin3.vi” (Figure F-2)
  - (c) Choose correct lock-in scale on “photocurrlockin3.vi”

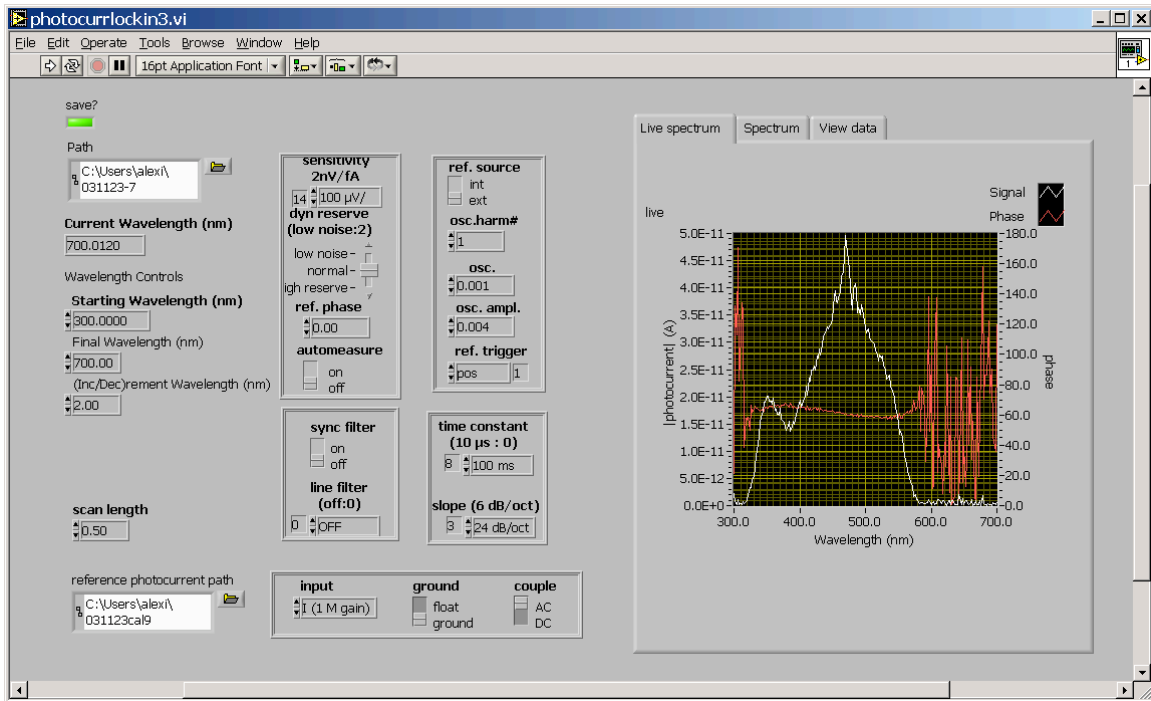


Figure F-2: LabView program “photocurrlockin3.vi” is used to measure the photocurrent spectrum

- (d) Type in path and filename to save
  - (e) Press play
7. Mount sample
    - (a) Place active area of sample at focal point of incident beam
    - (b) Connect sample to lock-in
    - (c) Set scale on lock-in appropriate to signal
  8. Take photocurrent spectrum
    - (a) Choose correct lock-in scale on “photocurrlockin3.vi”
    - (b) Type in path and filename to save
    - (c) Type in reference filename and path of previous calibration
    - (d) Press play
  9. Shutdown
    - (a) Set scale on lock-in to highest setting
    - (b) Turn off chopper
    - (c) Press lamp off button on lamp

- (d) Press power off on lamp
- (e) It is not necessary to power off the monochromator or lock-in



# Bibliography

- [1] S Coe, WK Woo, M Bawendi, and V Bulovic. Electroluminescence from single monolayers of nanocrystals in molecular organic devices. *NATURE*, 420(6917):800–803, 2002.
- [2] WU Huynh, JJ Dittmer, and AP Alivisatos. Hybrid nanorod-polymer solar cells. *SCIENCE*, 295(5564):2425–2427, 2002.
- [3] W Smith. Effect of light on selenium during passage of an electric current. *Nature*, 7(173):303, February 20 1873.
- [4] IEEE Electron Devices Society. 50 years of electron devices. <http://www.ieee.org/society/eds/>, 2002.
- [5] BEA Saleh and MC Teich. *Fundamentals of Photonics*. John Wiley and Sons, 1991.
- [6] A Rose. *Concepts in photoconductivity and applied problems*. Interscience publishers, 1963.
- [7] A Rogalski. Quantum well photoconductors in infrared detector technology. *JOURNAL OF APPLIED PHYSICS*, 93(8):4355–4391, 2003.
- [8] MA REED, JN RANDALL, RJ AGGARWAL, RJ MATYI, TM MOORE, and AE WETSEL. Observation of discrete electronic states in a zero-dimensional semiconductor nanostructure. *PHYSICAL REVIEW LETTERS*, 60(6):535–537, 1988.

- [9] V. Ryzhii, editor. *Intersubband Infrared Photodetectors*, volume 27. World Scientific, 2003.
- [10] J FAIST, F CAPASSO, DL SIVCO, C SIRTORI, AL HUTCHINSON, and AY CHO. Quantum cascade laser. *SCIENCE*, 264(5158):553–556, 1994.
- [11] DM MITTLEMAN, RW SCHOENLEIN, JJ SHIANG, VL COLVIN, AP ALIVISATOS, and CV SHANK. Quantum-size dependence of femtosecond electronic dephasing and vibrational dynamics in cdse nanocrystals. *PHYSICAL REVIEW B*, 49(20):14435–14447, 1994.
- [12] KF Brennan and J Haralson. Invited review - superlattice and multiquantum well avalanche photodetectors: physics, concepts and performance. *SUPERLATTICES AND MICROSTRUCTURES*, 28(2):77–104, 2000.
- [13] SR Forrest. Organic-inorganic semiconductor devices and 3, 4, 9, 10 perylenetetracarboxylic dianhydride: an early history of organic electronics. *JOURNAL OF PHYSICS-CONDENSED MATTER*, 15(38):S2599–S2610, 2003.
- [14] AP Alivisatos. Perspectives on the physical chemistry of semiconductor nanocrystals. *JOURNAL OF PHYSICAL CHEMISTRY*, 100(31):13226–13239, 1996.
- [15] R ROSSETTI, S NAKAHARA, and LE BRUS. Quantum size effects in the redox potentials, resonance raman-spectra, and electronic-spectra of cds crystallites in aqueous-solution. *JOURNAL OF CHEMICAL PHYSICS*, 79(2):1086–1088, 1983.
- [16] CB MURRAY, DJ NORRIS, and MG BAWENDI. Synthesis and characterization of nearly monodisperse cde (e=s, se, te) semiconductor nanocrystallites. *JOURNAL OF THE AMERICAN CHEMICAL SOCIETY*, 115(19):8706–8715, 1993.
- [17] NC Greenham, XG Peng, and AP Alivisatos. Charge separation and transport in conjugated-polymer/semiconductor-nanocrystal composites studied by



- photoluminescence quenching and photoconductivity. *PHYSICAL REVIEW B*, 54(24):17628–17637, 1996.
- [18] WU Huynh, JJ Dittmer, N Tecler, DJ Milliron, AP Alivisatos, and KWJ Barnham. Charge transport in hybrid nanorod-polymer composite photovoltaic cells. *PHYSICAL REVIEW B*, 67(11):–, 2003.
- [19] WU Huynh, XG Peng, and AP Alivisatos. Cdse nanocrystal rods/poly(3-hexylthiophene) composite photovoltaic devices. *ADVANCED MATERIALS*, 11(11):923–+, 1999.
- [20] WU Huynh, JJ Dittmer, WC Libby, GL Whiting, and AP Alivisatos. Controlling the morphology of nanocrystal-polymer composites for solar cells. *ADVANCED FUNCTIONAL MATERIALS*, 13(1):73–79, 2003.
- [21] BQ Sun, E Marx, and NC Greenham. Photovoltaic devices using blends of branched cdse nanoparticles and conjugated polymers. *NANO LETTERS*, 3(7):961–963, 2003.
- [22] DS Ginger and NC Greenham. Charge injection and transport in films of cdse nanocrystals. *JOURNAL OF APPLIED PHYSICS*, 87(3):1361–1368, 2000.
- [23] MV Jarosz, VJ Porter, BR Fisher, MA Kastner, and MG Bawendi. Photoconductivity studies of treated adse quantum dot films exhibiting increased exciton ionization efficiency. *to be published*, 2004.
- [24] BA Gregg. Bilayer molecular solar cells on spin-coated tio2 substrates. *CHEMICAL PHYSICS LETTERS*, 258(3-4):376–380, 1996.
- [25] K Kajihara, K Tanaka, K Hirao, and N Soga. Photovoltaic effect in titanium dioxide/zinc phthalocyanine cell. *JAPANESE JOURNAL OF APPLIED PHYSICS PART 1-REGULAR PAPERS SHORT NOTES REVIEW PAPERS*, 35(12A):6110–6116, 1996.
- [26] ZM Jarzebski. *Oxide Semiconductors*. Pergamon Press, 1973.

- [27] SM Sze. *Physics of Semiconductor Devices*. John Wiley and Sons, 1981.
- [28] BS Jeong, DP Norton, and JD Budai. Conductivity in transparent anatase tio2 films epitaxially grown by reactive sputtering deposition. *SOLID-STATE ELECTRONICS*, 47(12):2275–2278, 2003.
- [29] H TANG, K PRASAD, R SANJINES, PE SCHMID, and F LEVY. Electrical and optical-properties of tio2 anatase thin-films. *JOURNAL OF APPLIED PHYSICS*, 75(4):2042–2047, 1994.
- [30] MD Stamate. On the non-linear i-v characteristics of dc magnetron sputtered tio2 thin films. *APPLIED SURFACE SCIENCE*, 205(1-4):353–357, 2003.
- [31] B OREGAN and M GRATZEL. A low-cost, high-efficiency solar-cell based on dye-sensitized colloidal tio2 films. *NATURE*, 353(6346):737–740, 1991.
- [32] JR Durrant and SA Haque. Solar cells: A solid compromise. *NATURE MATERIALS*, 2(6):362–363, 2003.
- [33] P Wang, SM Zakeeruddin, JE Moser, MK Nazeeruddin, T Sekiguchi, and M Gratzel. A stable quasi-solid-state dye-sensitized solar cell with an amphiphilic ruthenium sensitizer and polymer gel electrolyte. *NATURE MATERIALS*, 2(6):402–407, 2003.
- [34] K Kajihara, K Tanaka, K Hirao, and N Soga. Photovoltaic effect in titanium dioxide/polythiophene cell. *JAPANESE JOURNAL OF APPLIED PHYSICS PART 1-REGULAR PAPERS SHORT NOTES REVIEW PAPERS*, 36(9A):5537–5542, 1997.
- [35] AC Arango, LR Johnson, VN Bliznyuk, Z Schlesinger, SA Carter, and HH Horhold. Efficient titanium oxide/conjugated polymer photovoltaics for solar energy conversion. *ADVANCED MATERIALS*, 12(22):1689–+, 2000.
- [36] AJ Breeze, Z Schlesinger, SA Carter, and PJ Brock. Charge transport in tio2/meh-ppv polymer photovoltaics. *PHYSICAL REVIEW B*, 6412(12):art. no.–125205, 2001.

- [37] CD Grant, AM Schwartzberg, GP Smestad, J Kowalik, LM Tolbert, and JZ Zhang. Optical and electrochemical characterization of poly (3-undecyl-2,2'-bithiophene) in thin film solid state tio<sub>2</sub> photovoltaic solar cells. *SYNTHETIC METALS*, 132(2):197–204, 2003.
- [38] KM Coakley, YX Liu, MD McGehee, KL Frindell, and GD Stucky. Infiltrating semiconducting polymers into self-assembled mesoporous titania films for photovoltaic applications. *ADVANCED FUNCTIONAL MATERIALS*, 13(4):301–306, 2003.
- [39] H Tokuhisa and PT Hammond. Solid-state photovoltaic thin films using tio<sub>2</sub>, organic dyes, and layer-by-layer polyelectrolyte nanocomposites. *ADVANCED FUNCTIONAL MATERIALS*, 13(11):831–839, 2003.
- [40] P HOYER and R KONENKAMP. Photoconduction in porous tio<sub>2</sub> sensitized by pbs quantum dots. *APPLIED PHYSICS LETTERS*, 66(3):349–351, 1995.
- [41] R Konenkamp, P Hoyer, and A Wahi. Heterojunctions and devices of colloidal semiconductor films and quantum dots. *JOURNAL OF APPLIED PHYSICS*, 79(9):7029–7035, 1996.
- [42] R Plass, S Pelet, J Krueger, M Gratzel, and U Bach. Quantum dot sensitization of organic-inorganic hybrid solar cells. *JOURNAL OF PHYSICAL CHEMISTRY B*, 106(31):7578–7580, 2002.
- [43] K Ernst, A Belaidi, and R Konenkamp. Solar cell with extremely thin absorber on highly structured substrate. *SEMICONDUCTOR SCIENCE AND TECHNOLOGY*, 18(6):475–479, 2003.
- [44] A Zaban, OI Micic, BA Gregg, and AJ Nozik. Photosensitization of nanoporous tio<sub>2</sub> electrodes with inp quantum dots. *LANGMUIR*, 14(12):3153–3156, 1998.
- [45] Q Shen and T Toyoda. Characterization of nanostructured tio<sub>2</sub> electrodes sensitized with cdse quantum dots using photoacoustic and photoelectrochemical

- current methods. *JAPANESE JOURNAL OF APPLIED PHYSICS PART 1-REGULAR PAPERS SHORT NOTES REVIEW PAPERS*, 43(5B):2946–2951, 2004.
- [46] R VOGEL, P HOYER, and H WELLER. Quantum-sized pbs, cds, ag<sub>2</sub>s, sb<sub>2</sub>s<sub>3</sub>, and bi<sub>2</sub>s<sub>3</sub> particles as sensitizers for various nanoporous wide-bandgap semiconductors. *JOURNAL OF PHYSICAL CHEMISTRY*, 98(12):3183–3188, 1994.
- [47] JL Blackburn, DC Selmarten, and AJ Nozik. Electron transfer dynamics in quantum dot/titanium dioxide composites formed by in situ chemical bath deposition. *JOURNAL OF PHYSICAL CHEMISTRY B*, 107(51):14154–14157, 2003.
- [48] DS Ginger and NC Greenham. Photoinduced electron transfer from conjugated polymers to cdse nanocrystals. *PHYSICAL REVIEW B*, 59(16):10622–10629, 1999.
- [49] M Drndic, MV Jarosz, NY Morgan, MA Kastner, and MG Bawendi. Transport properties of annealed cdse colloidal nanocrystal solids. *JOURNAL OF APPLIED PHYSICS*, 92(12):7498–7503, 2002.
- [50] BA Ridley, B Nivi, and JM Jacobson. All-inorganic field effect transistors fabricated by printing. *SCIENCE*, 286(5440):746–749, 1999.
- [51] P Peumans, A Yakimov, and SR Forrest. Small molecular weight organic thin-film photodetectors and solar cells, 2003.
- [52] AC Arango, SA Carter, and PJ Brock. Charge transfer in photovoltaics consisting of interpenetrating networks of conjugated polymer and tio<sub>2</sub> nanoparticles. *APPLIED PHYSICS LETTERS*, 74(12):1698–1700, 1999.
- [53] CM Ramsdale, JA Barker, AC Arias, JD MacKenzie, RH Friend, and NC Greenham. The origin of the open-circuit voltage in polyfluorene-based photovoltaic devices. *JOURNAL OF APPLIED PHYSICS*, 92(8):4266–4270, 2002.

- [54] BA Gregg. Excitonic solar cells. *JOURNAL OF PHYSICAL CHEMISTRY B*, 107(20):4688–4698, 2003.
- [55] AC Durr, F Schreiber, M Kelsch, HD Carstanjen, and H Dosch. Morphology and thermal stability of metal contacts on crystalline organic thin films. *ADVANCED MATERIALS*, 14(13-14):961–+, 2002.
- [56] EM Han, LM Do, M Fujihira, H Inada, and Y Shirota. Scanning force microscopy of organic thin-film amorphous hole transport materials. *JOURNAL OF APPLIED PHYSICS*, 80(6):3297–3305, 1996.